

# The Moving Discontinuous Galerkin Method with Interface Condition Enforcement for the Simulation of Hypersonic, Viscous Flows

Eric J. Ching, Andrew D. Kercher, Andrew Corrigan

*Laboratories for Computational Physics and Fluid Dynamics, U.S. Naval Research Laboratory, 4555 Overlook Ave SW, Washington, DC 20375*

---

## Abstract

The moving discontinuous Galerkin method with interface condition enforcement (MDG-ICE) is a high-order,  $r$ -adaptive method that treats the grid as a variable and weakly enforces the conservation law, constitutive law, and corresponding interface conditions in order to implicitly fit high-gradient flow features. In this paper, we develop an optimization solver based on the Levenberg-Marquardt algorithm that features an anisotropic, locally adaptive penalty method to enhance robustness and prevent cell degeneration in the computation of hypersonic, viscous flows. Specifically, we incorporate an anisotropic grid regularization based on the mesh-implied metric that inhibits grid motion in directions with small element length scales, an element shape regularization that inhibits nonlinear deformations of the high-order elements, and a penalty regularization that penalizes degenerate elements. Additionally, we introduce a procedure for locally scaling the regularization operators in an adaptive, elementwise manner in order to maintain grid validity. We apply the proposed MDG-ICE formulation to two- and three-dimensional test cases involving viscous shocks and/or boundary layers, including Mach 17.6 hypersonic viscous flow over a circular cylinder and Mach 5 hypersonic viscous flow over a sphere, which are very challenging test cases for conventional numerical schemes on simplicial grids. Even without artificial dissipation, the computed solutions are free from spurious oscillations and yield highly symmetric surface heat-flux profiles.

**Keywords:** Discontinuous Galerkin method; Interface condition enforcement; MDG-ICE; Implicit shock fitting; Anisotropic curvilinear  $r$ -adaptivity; Mesh adaptation

---

## 1. Introduction

The moving discontinuous Galerkin finite element method with interface condition enforcement (MDG-ICE) is an implicit shock fitting method capable of handling complex shock dynamics [1, 2, 3]. The method is a unique variation of the well-known discontinuous Galerkin (DG) method [4, 5]. Specifically, neighboring elements are not coupled through interfacial, single-valued numerical fluxes; instead, the conservation law and interface conditions (known as the generalized Rankine-Hugoniot jump conditions [6]) are directly discretized, and the grid is treated as a variable. By simultaneously solving for the flow field and discrete geometry, MDG-ICE is able to compute highly accurate high-order solutions *without artificial dissipation* as the grid points are automatically adjusted to fit shocks and resolve smooth regions of the flow with sharp gradients. This has significant advantages over traditional shock capturing approaches, such as artificial viscosity and limiting; the former introduces low-order errors into high-order approximations that can excessively smear discontinuous and high-gradient features (and even cause movement of such features that may then contaminate prediction of other flow structures [7]), while the latter can obstruct iterative convergence, fail to provide sufficient stabilization, and be used only for certain approximation orders and/or

element types. Furthermore, since MDG-ICE adapts the grid to satisfy the weak form, grid interfaces are naturally repositioned to fit a priori unknown shocks with arbitrary topology, overcoming key limitations of explicit shock fitting methods ([8, 9, 10]). Note that in the inviscid case, shocks are fit exactly along grid interfaces, while in the viscous setting, high-aspect-ratio cells form to resolve viscous shocks, which are sharp (yet smooth) features, via anisotropic curvilinear  $r$ -adaptivity. In previous work, MDG-ICE was shown to achieve not only extremely sharp, oscillation-free viscous-shock profiles, but also significantly higher accuracy than standard DG schemes in boundary-layer problems [2]. Another form of implicit shock fitting is the high-order implicit shock tracking (HOIST) framework developed by Zahr and Persson [11] and improved in [12, 13, 14, 15], which also treats the discrete geometry as a variable while retaining a standard discontinuous Galerkin method. High-quality solutions to inviscid flows with discontinuities on coarse grids have been achieved using HOIST. Additionally, a variant of MDG-ICE has been developed by Luo et al. [16].

Figure 1.1 presents the temperature fields and corresponding meshes for hypersonic viscous flow over a half-cylinder at Mach 5 and Reynolds number  $10^4$  on two-dimensional triangular grids. A DG( $\mathcal{P}_1$ ) solution (left), where  $\mathcal{P}_p$  denotes the space of polynomials of total degree  $p$  on simplicial elements, with artificial viscosity is compared with an isoparametric MDG-ICE( $\mathcal{P}_4$ ) solution (right) without any additional stabilization [2]. The corresponding meshes are also displayed. Unlike in the MDG-ICE solution, the shock in the DG solution is noticeably smeared, and spurious oscillations are visible both at the shock and in the shock layer. The resulting surface heating profile in the MDG-ICE solution is highly symmetric, which, despite the relatively simple flow conditions, is nevertheless encouraging since surface heat-flux predictions in state-of-the-practice finite-volume simulations of external hypersonic flows are known to deteriorate considerably when using simplicial grids [17, 18]. In particular, finite-volume schemes are extremely sensitive to misalignment between the grid and the shock and boundary layer, which generates errors in vorticity and entropy that propagate downstream and negatively impact the accuracy of computed surface quantities. Shock-tailored quadrilateral/hexahedral grids are typically needed to obtain heat-flux profiles that do not exhibit noticeable nonphysical asymmetries [19]. Constructing such grids for large-scale geometries often requires significant time and user effort [17, 19], which is exacerbated when performing parametric studies.

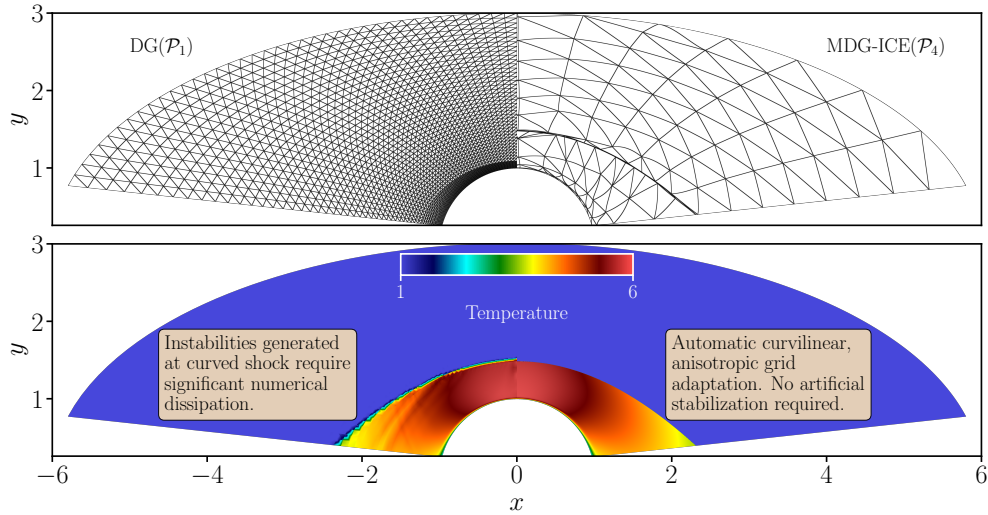


Figure 1.1: Comparison of DG( $\mathcal{P}_1$ ) (with artificial viscosity) (left) and MDG-ICE( $\mathcal{P}_4$ ) (right) solutions to two-dimensional Mach 5 flow over a cylinder at  $\text{Re} = 10^4$  [2]. The corresponding meshes are also displayed.

In contrast, implicit shock-fitting methods, such as MDG-ICE, automatically produce shock-aligned grids as part of the solution process, thereby mitigating the need for shock-tailored grids composed of cuboid elements, which significantly reduces the burden associated with generating a suitable grid for high-speed flow calculations. However, a major difficulty encountered in MDG-ICE calculations is frequent cell degeneration (i.e., the determinant of the geometric Jacobian becomes negative), particularly as curved,



high-aspect-ratio cells form to resolve sharp viscous features. Figure 1.2 displays the final mesh for an MDG-ICE solution to the same cylinder problem, but with a higher Reynolds number [2]. Degenerate cells were treated via longest-edge refinement, leading to the generation of “sliver” elements that introduce unnecessary degrees of freedom. Furthermore, although adequate for this relatively simple flow, in problems of moderately greater complexity, this strategy either requires an inordinate number of refinements or, worse, simply fails to recover a valid grid. Given this significant bottleneck precluding the application of MDG-ICE to more complicated, larger-scale configurations, the primary objective of this work is to develop an optimization solver that improves the robustness of the Levenberg-Marquardt algorithm employed in [2] and is capable of producing high-order approximations of hypersonic viscous flows in two and three dimensions without introducing low-order errors associated with artificial stabilization. The key feature of the solver is an anisotropic, locally adaptive penalty technique. In particular, we leverage the mesh-implied metric commonly employed in output-based anisotropic mesh adaptation [20, 21], which encodes information about the local element size and orientation (even on curved, anisotropic grids), to create an anisotropic grid regularization that inhibits grid motion in directions with small element length scales. This is similar to the inverse-volume scaling introduced by Zahr et al. [12] and employed in [3], but with element anisotropy explicitly taken into account. Furthermore, we incorporate additional regularization operators and develop an adaptive elementwise regularization strategy that locally adjusts regularization parameters as needed to maintain grid validity. We also employ increment limiting as described in [22], where the increment at each iteration is dynamically reduced to mitigate excessive changes in pressure and/or density. The improved solver, paired with a full parallelization of our MDG-ICE implementation, enables consideration of significantly more challenging hypersonic test cases. We specifically employ simplicial grids that are initially coarse with respect to the final high-gradient features in order to demonstrate the potential of MDG-ICE to greatly alleviate the burden of mesh generation on the user. Finally, we note that although incorporating artificial dissipation into the formulation in some capacity (e.g., applied only during intermediate iterations or minimally in the final solution) may be beneficial, the present study aims to aggressively test the underlying MDG-ICE formulation without the aid of additional stabilization and, as a secondary goal, identify in what ways stabilization would be most useful; incorporation of such dissipation mechanisms is left for future work.

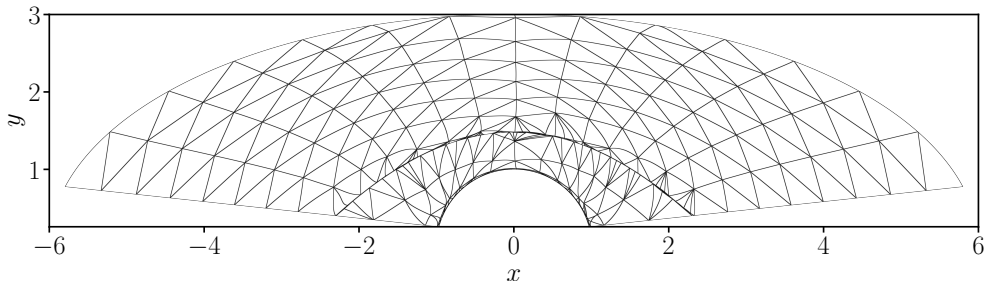


Figure 1.2: Final mesh for the isoparametric MDG-ICE( $\mathcal{P}_4$ ) solution to two-dimensional Mach 5 flow over a cylinder at  $\text{Re} = 10^5$  [2].

The remainder of this paper is organized as follows. Sections 2 and 3 briefly summarize the governing equations considered in this study and the basic MDG-ICE formulation, respectively. The improved optimization solver, which is the primary contribution of this work, is then detailed in Section 4. Section 5 presents solutions for a variety of challenging test cases, including two- and three-dimensional hypersonic viscous flows over blunt bodies in which surface heat flux is a target quantity. We conclude with final remarks and recommendations for future work.

## 2. Governing equations

Let  $\Omega \subset \mathbb{R}^d$  denote the domain, which can be either a space-time domain,  $\Omega \subset \mathbb{R}^{d=d_x+1}$ , or a spatial domain,  $\Omega \subset \mathbb{R}^{d=d_x}$ . Consider the following nonlinear conservation law governing the vector of  $m$  state

variables,  $y : \Omega \rightarrow \mathbb{R}^m$ :

$$\nabla \cdot \mathcal{F}(y, \nabla_x y) = 0 \text{ in } \Omega, \quad (2.1)$$

where  $\mathcal{F} : \mathbb{R}^m \times \mathbb{R}^{m \times d_x} \rightarrow \mathbb{R}^{m \times d}$  is the flux and  $\nabla_x(\cdot)$  denotes the spatial gradient,

$$\nabla_x y = \left( \frac{\partial y}{\partial x_1}, \dots, \frac{\partial y}{\partial x_{d_x}} \right). \quad (2.2)$$

In the case of a space-time domain (i.e.,  $d = d_x + 1$ ), the space-time flux is given by

$$\mathcal{F}(y, \nabla_x y) = (\mathcal{F}_1^x(y, \nabla_x y), \dots, \mathcal{F}_{d_x}^x(y, \nabla_x y), y), \quad (2.3)$$

where  $\mathcal{F}^x : \mathbb{R}^m \times \mathbb{R}^{m \times d_x} \rightarrow \mathbb{R}^{m \times d_x}$  is the spatial flux, defined as the difference between the convective flux and the viscous flux,

$$\mathcal{F}^x(y, \nabla_x y) = \mathcal{F}^c(y) - \mathcal{F}^v(y, \nabla_x y).$$

The divergence operator in Equation (2.1) is then the space-time divergence operator, given by

$$\nabla \cdot \mathcal{F}(y, \nabla_x y) = \nabla_x \cdot \mathcal{F}^x(y, \nabla_x y) + \frac{\partial}{\partial t} y. \quad (2.4)$$

In the case of a spatial domain (i.e.,  $d = d_x$ ), the flux is simply the spatial flux, and the divergence operator is the spatial divergence operator. In this study, we consider the viscous Burgers equation and the compressible Navier-Stokes equations.

### 2.1. One-dimensional viscous Burgers equation

The one-dimensional viscous Burgers equation involves a single state variable,  $y : \Omega \rightarrow \mathbb{R}^1$ . The convective and viscous fluxes are given by

$$\mathcal{F}^c(y) = \frac{1}{2} y^2, \quad \mathcal{F}^v(y, \nabla_x y) = \mu \nabla_x y, \quad (2.5)$$

where  $\mu \in \mathbb{R}_+$  is the viscosity. The spatial flux is then written as

$$\mathcal{F}^x(y, \nabla_x y) = \left( \frac{1}{2} y^2 - \mu \nabla_x y \right), \quad (2.6)$$

### 2.2. Compressible Navier-Stokes equations

The vector of state variables,  $y : \Omega \rightarrow \mathbb{R}^m$ , where  $m = d_x + 2$ , is given by

$$y = (\rho, \rho v_1, \dots, \rho v_{d_x}, \rho E), \quad (2.7)$$

where  $\rho : \Omega \rightarrow \mathbb{R}_+$  is the density,  $v = (v_1, \dots, v_{d_x})$  is the velocity vector, with  $v : \mathbb{R}^m \rightarrow \mathbb{R}^{d_x}$ , and  $E : \mathbb{R}^m \rightarrow \mathbb{R}_+$  is the specific total energy. The  $i$ th spatial component of the convective flux is written as

$$\mathcal{F}_i^c(y) = (\rho v_i, \rho v_i v_1 + P \delta_{i1}, \dots, \rho v_i v_{d_x} + P \delta_{id_x}, \rho H v_i), \quad (2.8)$$

where  $P : \mathbb{R}^m \rightarrow \mathbb{R}_+$  is the pressure,  $\delta_{ij}$  is the Kronecker delta, and  $H = (\rho E + P) / \rho$  is the specific total enthalpy, with  $H : \mathbb{R}^m \rightarrow \mathbb{R}_+$ . In this work, we assume a calorically perfect gas, such that

$$P = (\gamma - 1) \left( \rho E - \frac{1}{2} \sum_{i=1}^{d_x} \rho v_i v_i \right), \quad (2.9)$$

where  $\gamma$  is the specific heat ratio, set to 1.4. Note that the assumption of a single-species calorically perfect gas is appropriate for evaluating the capability of a numerical method to handle sharp, high-gradient features

such as strong shocks and boundary layers, although more complex gas and transport models are typically employed in realistic hypersonic applications [23].

The  $i$ th spatial component of the viscous flux is written as

$$\mathcal{F}_i^\nu(y, \nabla_x y) = \left( 0, \tau_{1i}, \dots, \tau_{d_x i}, \sum_{j=1}^{d_x} \tau_{ij} v_j - q_i \right), \quad (2.10)$$

where  $q : \mathbb{R}^m \times \mathbb{R}^{m \times d_x} \rightarrow \mathbb{R}^{d_x}$  is the heat flux and  $\tau : \mathbb{R}^m \times \mathbb{R}^{m \times d_x} \rightarrow \mathbb{R}^{d_x \times d_x}$  is the viscous stress tensor. The heat flux is expanded as  $q = -\kappa \nabla_x T$ , where  $\kappa : \mathbb{R}^m \rightarrow \mathbb{R}_+$  is the thermal conductivity and  $T : \mathbb{R}^m \rightarrow \mathbb{R}_+$  is the temperature, calculated as  $T = P/(\rho R)$ , with  $R = 287$  denoting the specific gas constant. The  $i$ th spatial component of the viscous stress tensor is given by

$$\tau_i = \mu \left( \frac{\partial v_1}{\partial x_i} + \frac{\partial v_i}{\partial x_1} - \delta_{i1} \frac{2}{3} \sum_{j=1}^{d_x} \frac{\partial v_j}{\partial x_j}, \dots, \frac{\partial v_{d_x}}{\partial x_i} + \frac{\partial v_i}{\partial x_{d_x}} - \delta_{id_x} \frac{2}{3} \sum_{j=1}^{d_x} \frac{\partial v_j}{\partial x_j} \right), \quad (2.11)$$

where  $\mu : \mathbb{R}^m \rightarrow \mathbb{R}_+$  is the dynamic viscosity obtained from Sutherland's law,

$$\mu = \mu_0 \frac{T_0 + C}{T + C} \left( \frac{T}{T_0} \right)^{\frac{3}{2}}. \quad (2.12)$$

$u_0 \in \mathbb{R}_+$  is the reference dynamic viscosity, and  $T_0 \in \mathbb{R}_+$  and  $C \in \mathbb{R}_+$  are reference temperatures. Nondimensionalizing Equation (2.12) using freestream quantities, denoted  $(\cdot)_\infty$ , yields

$$\mu^* = \frac{1 + C^*}{T^* + C^*} (T^*)^{\frac{3}{2}}, \quad (2.13)$$

where  $\mu^* = \mu/\mu_\infty$ ,  $T^* = T/T_\infty$ , and  $C^* = C/T_\infty$ . In this study, we use  $C = 110$  K and  $T_\infty = 293.15$  K. The thermal conductivity is computed as

$$k = \frac{c_p \mu}{\text{Pr}}, \quad (2.14)$$

where  $\text{Pr} = 0.72$  is the Prandtl number and  $c_p = \gamma R/(\gamma - 1)$  is the specific heat capacity at constant pressure.

Two important nondimensional quantities that characterize compressible, viscous flows are the Reynolds number,  $\text{Re}$ , and Mach number,  $\text{Ma}$ , defined as

$$\text{Re} = \frac{\rho |v| L}{\mu}, \quad (2.15)$$

where  $L \in \mathbb{R}_+$  is a characteristic length scale, and

$$\text{Ma} = \frac{|v|}{c}, \quad (2.16)$$

where  $c = \sqrt{\gamma P/\rho}$  is the speed of sound, with  $c : \mathbb{R}^m \rightarrow \mathbb{R}_+$ , respectively.

### 3. Moving discontinuous Galerkin method with interface condition enforcement

In this subsection, we briefly review the MDG-ICE formulation for a system governed by a set of conservation laws and a generalized constitutive law. Further details regarding the formulation and its application can be found in [2], and an alternative least-squares formulation is described in [3].

Let  $\Omega$  be partitioned by  $\mathcal{T}$ , which consists of cells  $\kappa$ . Furthermore, we define the set  $\mathcal{E}$  of interfaces such that  $\bigcup_{\epsilon \in \mathcal{E}} = \bigcup_{\kappa \in \mathcal{T}} \partial \kappa$ . The normal over each interface  $\epsilon \in \mathcal{E}$  is denoted  $n : \epsilon \rightarrow \mathbb{R}^d$ . For space-time domains,  $n_x : \epsilon \rightarrow \mathbb{R}^{d_x}$  denotes the spatial normal.

### 3.1. Strong and weak formulations

Consider the following conservation law, constitutive law, and associated interface conditions in strong form:

$$\nabla \cdot \mathcal{F}(y, \sigma) = 0 \text{ in } \kappa \quad \forall \kappa \in \mathcal{T}, \quad (3.1)$$

$$\sigma - G(y) \nabla_x y = 0 \text{ in } \kappa \quad \forall \kappa \in \mathcal{T}, \quad (3.2)$$

$$\llbracket n \cdot \mathcal{F}(y, \sigma) \rrbracket = 0 \text{ on } \epsilon \quad \forall \epsilon \in \mathcal{E}, \quad (3.3)$$

$$\llbracket G(y) \rrbracket \llbracket y \otimes n_x \rrbracket = 0 \text{ on } \epsilon \quad \forall \epsilon \in \mathcal{E}, \quad (3.4)$$

where  $\sigma : \Omega \rightarrow \mathbb{R}^{m \times d_x}$  is an auxiliary variable,  $G(y) \in \mathbb{R}^{m \times d_x \times m \times d_x}$  is the homogeneity tensor that satisfies  $G(y) \nabla_x y = \mathcal{F}^v(y, \nabla_x y) = \mathcal{F}_{\nabla_x y}^v(y, \nabla_x y) \nabla_x y$  (assuming the viscous flux is linear with respect to the spatial gradient of the state), and  $\{\cdot\}$  and  $\llbracket \cdot \rrbracket$  denote the average and jump operators, respectively. The interface condition (3.3), which corresponds to the conservation law (3.1), is known as the jump or generalized Rankine-Hugoniot conditions [6]. The interface condition (3.4), derived in [2], is associated with the constitutive law (3.2) and constrains the continuity of the state variable at the interface.

Let the solution spaces  $Y$  and  $\Sigma$  be the broken Sobolev spaces

$$Y = \left\{ y \in [L^2(\Omega)]^m \mid \forall \kappa \in \mathcal{T}, \quad y|_{\kappa} \in [H^1(\kappa)]^m \right\}, \quad (3.5)$$

$$\Sigma = \left\{ \sigma \in [L^2(\Omega)]^{m \times d_x} \mid \forall \kappa \in \mathcal{T}, \quad \nabla_x \cdot \sigma|_{\kappa} \in [L^2(\Omega)]^m \right\}. \quad (3.6)$$

The MDG-ICE weak formulation is then obtained by integrating Equations (3.1)-(3.4) against separate test functions: find  $(y, \sigma) \in Y \times \Sigma$  such that

$$\begin{aligned} 0 = & \sum_{\kappa \in \mathcal{T}} (\nabla \cdot \mathcal{F}(y, \sigma), v_y)_{\kappa} \\ & + \sum_{\kappa \in \mathcal{T}} (\sigma - G(y) \nabla_x y, v_{\sigma})_{\kappa} \\ & - \sum_{\epsilon \in \mathcal{E}} (\llbracket n \cdot \mathcal{F}(y, \sigma) \rrbracket, w_y)_{\epsilon} \\ & - \sum_{\epsilon \in \mathcal{E}} (\llbracket G(y) \rrbracket \llbracket y \otimes n_x \rrbracket, w_{\sigma})_{\epsilon} \quad \forall (v_y, v_{\sigma}, w_y, w_{\sigma}) \in V_y \times V_{\sigma} \times W_y \times W_{\sigma}. \end{aligned} \quad (3.7)$$

where the test spaces are  $V_y = [L^2(\Omega)]^m$  and  $V_{\sigma} = [L^2(\Omega)]^{m \times d}$ , with  $W_y$  and  $W_{\sigma}$  defined as the corresponding single-valued trace spaces. Note that numerical flux functions are not employed in the current MDG-ICE formulation, although with slight modifications, it is straightforward to include them [1].

To treat the grid as a variable, the weak formulation (3.7) is transformed from physical to reference space. Let  $u : \hat{\Omega} \rightarrow \Omega$  be a continuous, invertible mapping from the reference domain,  $\hat{\Omega}$ , to the physical domain,  $\Omega$ .  $\hat{\Omega}$  is assumed to be partitioned by  $\hat{\mathcal{T}}$ , such that  $\hat{\Omega} = \cup_{\hat{\kappa} \in \hat{\mathcal{T}}} \hat{\kappa}$ . Furthermore, let  $\hat{\mathcal{E}}$  denote the set of interfaces,  $\hat{\epsilon}$ , such that  $\cup_{\hat{\epsilon} \in \hat{\mathcal{E}}} \hat{\epsilon} = \cup_{\hat{\kappa} \in \hat{\mathcal{T}}} \partial \hat{\kappa}$ , and let  $U = \left[ H^1(\hat{\Omega}) \right]^d$ , the  $\mathbb{R}^d$ -valued Sobolev space over  $\hat{\Omega}$ . The solution and test spaces are also now assumed to be defined over reference space. We then define a

provisional state operator,  $\tilde{e} : Y \times \Sigma \times U \rightarrow (V_y \times V_\sigma \times W_y \times W_\sigma)^*$  for  $(y, \sigma, u) \in Y \times \Sigma \times U$ , as

$$\begin{aligned} \tilde{e}(y, \sigma, u) = (v_y, v_\sigma, w_y, w_\sigma) \mapsto & \sum_{\hat{\kappa} \in \hat{\mathcal{T}}} ((\text{cof}(\nabla u) \nabla) \cdot \mathcal{F}(y, \sigma), v_y)_{\hat{\kappa}} \\ & + \sum_{\hat{\kappa} \in \hat{\mathcal{T}}} (\det(\nabla u) \sigma - G(y) (\text{cof}(\nabla u) \nabla)_x y, v_\sigma)_{\hat{\kappa}} \\ & - \sum_{\hat{e} \in \hat{\mathcal{E}}} (\llbracket s(\nabla u) \cdot \mathcal{F}(y, \sigma) \rrbracket, w_y)_{\hat{e}} \\ & - \sum_{\hat{e} \in \hat{\mathcal{E}}} (\llbracket G(y) \rrbracket \llbracket y \otimes s(\nabla u)_x \rrbracket, w_\sigma)_{\hat{e}}. \end{aligned} \quad (3.8)$$

The state operator,  $e : Y \times \Sigma \times U \rightarrow (V_y \times V_\sigma \times W_y \times W_\sigma)^*$ , is defined as

$$e(y, \sigma, u) = \tilde{e}(y, \sigma, b(u)), \quad (3.9)$$

which imposes geometric boundary conditions via the geometric projection operator,  $b(u)$ .

The state equation in reference space is  $e(y, \sigma, u) = 0$ , such that the corresponding weak formulation in reference space is as follows: find  $(y, \sigma, u) \in Y \times \Sigma \times U$  such that

$$\langle e(y, \sigma, u), (v_y, v_\sigma, w_y, w_\sigma) \rangle = 0 \quad \forall (v_y, v_\sigma, w_y, w_\sigma) \in V_y \times V_\sigma \times W_y \times W_\sigma. \quad (3.10)$$

The solution is therefore given by  $(y, \sigma, b(u)) \in Y \times \Sigma \times U$ .

### 3.2. Discretization

To discretize the weak formulation (3.10), we choose discrete subspaces  $Y_h \subset Y$ ,  $\Sigma_h \subset \Sigma$ ,  $U_h \subset U$ ,  $V_{y,h} \subset V_y$ ,  $V_{\sigma,h} \subset V_\sigma$ ,  $W_{y,h} \subset W_y$ , and  $W_{\sigma,h} \subset W_\sigma$  and define a discrete state operator

$$e_h : Y_h \times \Sigma_h \times U_h \rightarrow \mathbb{R}^{\dim(V_{y,h} \times V_{\sigma,h} \times W_{y,h} \times W_{\sigma,h})}. \quad (3.11)$$

For a simplicial grid,

$$Y_h = \left\{ y \in Y \mid \forall \hat{\kappa} \in \hat{\mathcal{T}}, y|_{\hat{\kappa}} \in [\mathcal{P}_p]^m \right\}, \quad (3.12)$$

$$\Sigma_h = \left\{ \sigma \in \Sigma \mid \forall \hat{\kappa} \in \hat{\mathcal{T}}, \sigma|_{\hat{\kappa}} \in [\mathcal{P}_p]^{m \times d_x} \right\}, \quad (3.13)$$

where  $\mathcal{P}_p$  is the space of polynomials spanned by the monomials  $\mathbf{x}^\beta$  with multi-index  $\beta \in \mathbb{N}_0^d$  satisfying  $\sum_{i=1}^d \beta_i \leq p$ . We set  $V_{y,h} = Y_h$  and  $V_{\sigma,h} = \Sigma_h$ .  $W_{y,h}$  and  $W_{\sigma,h}$  are selected to be the corresponding single-valued polynomial trace spaces. The discrete subspace  $U_h$  of geometric mappings is defined as

$$U_h = \left\{ u \in U \mid \forall \hat{\kappa} \in \hat{\mathcal{T}}, u|_{\hat{\kappa}} \in [\mathcal{P}_p]^d \right\}. \quad (3.14)$$

In this work, the polynomial degrees of  $Y_h$  and  $\Sigma_h$  are chosen to be equal; the polynomial degree of  $U_h$ , however, may be different. The cases in which the polynomial degree of  $U_h$  is greater than, the same as, and less than the polynomial degrees of  $Y_h$  and  $\Sigma_h$  are referred to as superparametric, isoparametric, and subparametric, respectively.

## 4. Nonlinear solver

The nonlinear solver developed for this work is based on the Levenberg-Marquardt method that was previously employed [2], in which the weak formulation is solved iteratively (in nondimensional form) using unconstrained optimization to minimize the objective function

$$J(y, \sigma, u) = \frac{1}{2} \|e_h(y, \sigma, u)\|^2 \quad (4.1)$$

by seeking a stationary point

$$\nabla J(y, \sigma, u) = e'_h(y, \sigma, u)^* e_h(y, \sigma, u) = 0, \quad (4.2)$$

where  $e'_h(y, \sigma, u)^* : \mathbb{R}^{\dim(V_{y,h} \times V_{\sigma,h} \times W_{y,h} \times W_{\sigma,h})} \rightarrow Y_h \times \Sigma_h \times U_h$  is the adjoint operator. Given an initialization  $(y, \sigma, u)_0$ , the solution is repeatedly updated

$$(y, \sigma, u)_{i+1} = (y, \sigma, u)_i + \Delta(y, \sigma, u)_i \quad i = 0, 1, 2, \dots \quad (4.3)$$

until (4.2) is satisfied to a given tolerance. The Levenberg-Marquardt method [24, 25] is then employed to solve (4.2), which yields the increment

$$\Delta(y, \sigma, u) = - (e'_h(y, \sigma, u)^* e'_h(y, \sigma, u) + I_{h,\lambda}(y, \sigma, u))^{-1} (e'_h(y, \sigma, u)^* e_h(y, \sigma, u)), \quad (4.4)$$

where  $I_{h,\lambda}(y, \sigma, u) : (Y_h \times \Sigma_h \times U_h) \times (Y_h \times \Sigma_h \times U_h) \rightarrow \mathbb{R}$  is a symmetric, positive-definite bilinear form that defines the choice of regularization

$$I_{h,\lambda}(y, \sigma, u)((\delta y, \delta \sigma, \delta u), (v_y, v_\sigma, v_u)) = (\delta y, \lambda_y v_y) + (\delta \sigma, \lambda_\sigma v_\sigma) + (\delta u, \lambda_u v_u). \quad (4.5)$$

with  $\lambda_y$ ,  $\lambda_\sigma$ , and  $\lambda_u$  denoting nonnegative regularization coefficients for each solution variable. In practice,  $\lambda_y$  and  $\lambda_\sigma$  are set to zero. In addition to the identity regularization (4.5), which ensures positive definiteness and prevents large-scale grid changes, we incorporate a Laplacian-type grid regularization,

$$I_{h,\lambda}^\Delta(y, \sigma, u)((\delta y, \delta \sigma, \delta u), (v_y, v_\sigma, v_u)) = -(\nabla(b'_h(u)\delta u), \lambda_{\Delta u} \nabla(b'_h(u)v_u)). \quad (4.6)$$

where  $\lambda_{\Delta u} \geq 0$  is the corresponding regularization coefficient and  $v_u \in U_h$ , which introduces a compressibility effect into the grid motion. In previous work [3], following the approach of Zahr et al. [12], the regularization factor  $\lambda_{\Delta u}$  was modified to incorporate a factor proportional to the inverse of the element volume, which locally stiffens small elements in an *isotropic* manner. Note that the regularizations (4.5) and (4.6) are not incorporated into the objective function (4.1).

The solver as hitherto described was employed in [2]. In the remainder of this section, we introduce enhancements to the solver that significantly improve its robustness.

#### 4.1. Regularization terms

##### 4.1.1. Anisotropic Laplacian-type grid regularization

In this work, we modify the regularization (4.6) to directly account for element anisotropy as

$$I_{h,\lambda}^\Delta(y, \sigma, u)((\delta y, \delta \sigma, \delta u), (v_y, v_\sigma, v_u)) = -\left(\nabla\left(\mathcal{H}^{-\alpha/2} b'_h(u) \delta u\right), \lambda_{\Delta u} \nabla\left(\mathcal{H}^{-\alpha/2} b'_h(u) v_u\right)\right), \quad (4.7)$$

where  $\alpha \geq 0$  is a parameter and  $\mathcal{H}$ , in the two-dimensional case, is an element-local,  $2 \times 2$ , symmetric-positive-definite transformation matrix given by [20, 26]

$$\mathcal{H} = \mathcal{M}^{-1/2} = V \Sigma V^T = \begin{bmatrix} | & | \\ \hat{e}_1 & \hat{e}_2 \\ | & | \end{bmatrix} \begin{bmatrix} h_1 & 0 \\ 0 & h_2 \end{bmatrix} \begin{bmatrix} - & \hat{e}_1^T & - \\ - & \hat{e}_2^T & - \end{bmatrix}. \quad (4.8)$$

$\mathcal{M}$  is the metric implied by the mesh [20], the columns of  $V$  are the (orthonormal) left singular vectors,  $\hat{e}_1$  and  $\hat{e}_2$ , of the geometric Jacobian,  $J$ , and  $\Sigma$  is a diagonal matrix with the singular values,  $h_1$  and  $h_2$ , of  $J$  along the main diagonal.  $\mathcal{H}$  projects the unit circle to an ellipse with principal directions  $\hat{e}_1$  and  $\hat{e}_2$  and principal stretching magnitudes  $h_1$  and  $h_2$  [26]. Without loss of generality, we assume that the singular values are ordered such that  $h_1 \leq h_2$ .  $\mathcal{H}^{-\alpha}$  can be expanded as

$$\mathcal{H}^{-\alpha} = V \Sigma^{-\alpha} V^T = \begin{bmatrix} | & | \\ \hat{e}_1 & \hat{e}_2 \\ | & | \end{bmatrix} \begin{bmatrix} h_1^{-\alpha} & 0 \\ 0 & h_2^{-\alpha} \end{bmatrix} \begin{bmatrix} - & \hat{e}_1^T & - \\ - & \hat{e}_2^T & - \end{bmatrix}. \quad (4.9)$$

As such, the modified regularization (4.7) limits grid motion in directions with small element length scales while allowing for greater changes in directions with larger length scales, aiding in the formation of non-degenerate high-aspect-ratio elements to resolve thin viscous structures. For simplicity,  $\mathcal{H}^{-\alpha}$  is evaluated at the centroid of the given element. The metric described here is a powerful tool that can be used not only for anisotropic grid regularization but also for remeshing via a metric-based grid generator [20] in order to maintain high-quality grids, which will be the subject of future work. Moreover, we employ additional regularization operators that further inhibit element degeneration, specifically  $\mathcal{P}_1$  grid regularization and penalty grid regularization, which are described below. Similar forms of these two regularization operators were employed in the mesh untangling algorithm by Toulorge et al. [27].

#### 4.1.2. $\mathcal{P}_1$ grid regularization

To penalize excessive element curvature, the following regularization term is included in the objective function (4.1):

$$J_1(u) = \frac{1}{2} h_1^\beta \lambda_1 \|u - \Pi_1 u\|^2, \quad (4.10)$$

where  $\lambda_1$  is the corresponding regularization coefficient,  $h_1$  is obtained from the mesh-implied metric,  $\Pi_1$  denotes the projection to a (multi-)linear subspace of  $U_h$ , and  $\beta > 0$  is a parameter. The  $h_1^\beta$  scaling allows for increased curvature of elements with small length scales, which is important for resolving curved shocks.

#### 4.1.3. Penalty grid regularization

Finally, a penalty regularization term is included in the objective function (4.1):

$$J_b(u) = \frac{1}{2} \lambda_b \|f(u)\|^2, \quad (4.11)$$

where  $\lambda_b$  is the corresponding regularization coefficient and  $f$  is defined as

$$f(u) = \max\{0, \mathcal{J}_b - \det(\nabla u)\}, \quad (4.12)$$

with  $\mathcal{J}_b$  represents a desired lower bound on the Jacobian determinant (e.g.,  $10^{-10}$ ). The regularization (4.11) penalizes invalid elements (i.e., elements for which the determinant of the geometric Jacobian is nonpositive). Note that the non-differentiability of  $f(u)$  at  $\det(\nabla u) = \mathcal{J}_b$  is not found to cause any noticeable issues; furthermore, it can easily be made differentiable by squaring the RHS of (4.12). In previous work [1], barrier grid regularization was found to frequently lead to solver stagnation, although such regularization may nevertheless be worthy of future investigation.

#### 4.1.4. Global scaling

In this work, the regularization coefficients  $\lambda_u$ ,  $\lambda_{\Delta u}$ ,  $\lambda_1$ , and  $\lambda_b$  are scaled by the residual magnitude,  $\|e_h(y, \sigma, u)\|$ . Early in the simulation, when the residual is large and spurious transients may appear in the solution, the higher regularization prevents excessive grid changes that would otherwise occur. As the solution converges and these transients disappear, the lower regularization encourages greater adjustments to the grid to facilitate resolution of high-gradient features. To prevent rank deficiency of the linear system at low residuals, we select a small, positive number as a lower bound on  $\lambda_u$  (e.g.,  $10^{-7}$ ).

#### 4.2. Adaptive, elementwise regularization

Even with manual tuning, the aforementioned global, static scaling of the regularization terms is not sufficiently robust for preventing cell degeneration, especially as highly anisotropic, curved elements form to resolve multidimensional, high-gradient features. Local grid operations, whether topology-preserving (e.g., vertex smoothing [28]) or topology-changing (e.g., edge refinement, collapse [29], and swapping [28]), may be beneficial if used sparingly; however, such operations often fail to recover valid cells and will inhibit iterative convergence of the solver since they are not intrinsic to the formulation (i.e., they are applied as a “postprocessing” step at the end of the iteration). This obstruction of convergence is exacerbated



in the viscous setting, wherein high-aspect-ratio elements are gradually compressed to better resolve thin viscous structures. Mesh deformation techniques have also been developed to improve mesh quality and untangle invalid elements, typically in the context of a posteriori high-order mesh generation. Examples include elasticity-based methods [30, 31, 32], in which a set of elasticity equations is solved to obtain a mesh-displacement field, and mesh optimization algorithms [27, 33], which seek to minimize element distortion and constrain invalid Jacobians via regularization operators similar to (4.10) and (4.11). Although more reliable for recovering valid elements and potentially useful for occasionally “resetting” the grid in case convergence begins to stall, these mesh-deformation techniques can be expensive and again disrupt solver convergence, especially because they need to be engaged frequently in the presence of curved, high-gradient features. Incorporating regularization operators directly into the objective function (4.1) eliminates, or at least mitigates, obstruction of iterative convergence, but, as previously mentioned, global, static scaling of the regularization terms does not provide sufficient robustness.

In light of the above, we propose a strategy for maintaining grid validity that can reliably recover valid cells while avoiding disruption of solver convergence. In particular, when a cell becomes invalid, the iteration is restarted (i.e., the solution is “rolled back”) and the regularization coefficients are automatically adjusted in an elementwise fashion until the solver can proceed with a valid grid. In this work,  $\lambda_{\Delta u}$ ,  $\lambda_1$ , and  $\lambda_b$  are dynamically scaled; however, if the aspect ratio is high (e.g.,  $h_2/h_1 > 10$ ), then  $\lambda_1$  is left unchanged in order to facilitate resolution of thin, curved features using curved cells. The regularization coefficients are then successively decreased to their base values, unless the element once again becomes invalid. The rollback of the solution is crucial for ensuring a valid grid at every iteration. Although our formulation does not necessarily diverge in the presence of (slightly) negative Jacobian determinants, maintaining grid validity at every iteration is important for the following reasons: (a) allowing the solver to proceed with invalid cells can result in pollution of solution accuracy and lower-quality grids that may drive the solution towards a less-optimal local minimum; (b) in our experience, once the solver proceeds with negative Jacobian determinants, it can be extremely difficult to eliminate them; and (c) if negative Jacobian determinants become too large in magnitude, the solver can easily diverge or at least produce clearly erroneous results. Furthermore, although the intermittent scaling of the penalty grid regularization can cause abrupt increases in the objective function (specifically,  $J_b$ ), this is not a major concern since we are ultimately interested in minimizing  $\|e_h(y, \sigma, u)\|$ . This adaptive, elementwise regularization strategy is found to be critical for preventing cell degeneration in the vicinity of viscous shocks and boundary layers at hypersonic flow conditions. With such high-gradient features, zero to three rollbacks per iteration are typically required to preserve grid validity. Note that if the solution is rolled back, only the regularization terms for the corresponding cells need to be recomputed. The implementation details of this strategy will be provided in Section 4.4.

#### 4.3. Increment limiting

The consideration of very strong shocks without artificial dissipation often leads to undershoots and overshoots in pressure and other quantities during intermediate iterations. To mitigate these instabilities, which can otherwise cause solver divergence, we employ an increment-limiting strategy used in standard implicit-DG solvers [22], in which the increment is scaled by a factor no greater than unity such that the maximum change in pressure and density at the integration points is less than a user-specified fraction, denoted  $f$  (e.g.,  $f = 10\%$ ). The implementation details will be provided in Section 4.4.

We have also experimented with projecting the state in troubled elements to a first-order approximation ( $\mathcal{P}_0$ ), but this can hinder iterative convergence by creating a cycle in which first-order projections are followed by eventual reappearance of undershoots/overshoots, which then causes additional first-order projections, and so on. Applying sophisticated limiters that, for example, nominally preserve order of accuracy to troubled elements during intermediate iterations may also be useful, but is not considered in this work.

#### 4.4. Line search

The locally adaptive regularization and increment limiting discussed in Sections 4.2 and 4.3, respectively are incorporated into a simple line search method, as presented in Algorithm 1. It should be noted that decreasing  $\|e_h(y, \sigma, u)\|$  and maintaining grid validity (i.e., minimizing  $J_b$ ) are often at odds with each other

Table 1: Recommended base values for regularization coefficients and other parameters

$\lambda_u$	$\lambda_{\Delta u}$	$\lambda_1$	$\lambda_b$	$\mathcal{J}_b$	$\alpha$	$\beta$
$10^{-7}$	$10^{-5}$	$10^{-3}$	$10^2$	$10^{-10}$	-1	3

since penalizing small Jacobian determinants can hinder resolution of high-gradient features, especially those which are curved. Penalty regularization is thus activated only when necessary and in a local, gradual fashion in order to avoid interfering with reduction of  $\|e_h(y, \sigma, u)\|$  and potential convergence towards a less optimal local minimum. The local regularization coefficients  $\lambda_{\Delta u}^\kappa$ ,  $\lambda_1^\kappa$ , and  $\lambda_b^\kappa$  are then successively decreased every few steps towards their base values and  $\mathcal{J}_b^\kappa$  is reset, provided that the given element remains valid. Recommended base values for the regularization coefficients and other parameters are given in Table 1. We also find that even though scaling the regularization coefficients by  $\|e_h(y, \sigma, u)\|$  is often beneficial, sometimes, at low values of  $\|e_h(y, \sigma, u)\|$ , the grid has already repositioned itself enough to resolve the anisotropic structures in the flow, at which point anything more than marginal adjustments to the grid can slow down residual convergence. To minimize grid motion in this situation,  $\lambda_u$  and  $\lambda_{\Delta u}$  are automatically scaled in a global fashion by factors of 100 for a prescribed number of iterations (e.g., 30) when repeatedly low values of the increment factor (e.g.,  $\omega < 0.02$ ) are accompanied by at least one rollback, which serves as a reliable indicator of said scenario.

Note that modifying the hard-coded values in Algorithm 1 (e.g., setting  $N_{\text{search}}$  to five and scaling  $\lambda_{\Delta u}^\kappa$  by a factor of ten) can potentially yield better performance; nevertheless, the chosen values work sufficiently well for the problems considered in this study, and we remark that the primary concern of this work is robustness in terms of maintaining grid validity. Future work will explore strategies to accelerate iterative convergence, as well as well-established methods to automatically adjust the global values of  $\lambda_u$  and/or  $\lambda_{\Delta u}$  at each step [34, 12]. Furthermore, similar results can likely be obtained with locally adaptive barrier functions (as opposed to penalty functions), although as previously mentioned, a naive strategy may lead to frequent solver stagnation. In addition, though not employed here, it may be useful to activate penalty regularization over a localized region of elements, instead of just one element, since doing so for only one element can lead to movement of grid points that then causes degeneration in neighboring cells.

Finally, we remark that the full system can also be explicitly formulated as a constrained-optimization problem with inequality constraints  $\det(\nabla u) > 0$ , where Lagrange multipliers corresponding to those constraints are introduced as solution variables. Although future work may explore a Lagrange-multiplier approach, the proposed unconstrained-optimization formulation is appealing due to its simplicity and smaller system size.

## 5. Results

We apply MDG-ICE, equipped with the enhanced nonlinear solver described in Section 4, to compute viscous flows with high-gradient features. Unsteady solutions are obtained using a space-time discretization. All grids are generated using Gmsh [35]. The simulations in this study are performed using the JENRE® Multiphysics Framework employed in previous work [1, 2, 3] with the modifications and extensions described here. The three-dimensional solutions are computed using hybrid shared- and distributed-memory parallelism, the latter of which was not implemented in previous work. In the present study, we employ a sparse, direct LDLT solver provided by the MUMPS (MULTifrontal Massively Parallel Solver) package [36, 37] via the PETSc (Portable, Extensible Toolkit for Scientific Computation) software library [38, 39]. Future work will improve the efficiency of solving the linear system by leveraging techniques such as domain decomposition and multigrid algorithms.

### 5.1. Space-time Burgers viscous shock formation

This section presents results for space-time Burgers viscous shock formation, previously computed using MDG-ICE in [2]. The initial condition is given by

---

**Algorithm 1** Line search algorithm for iteration  $i + 1$ .  $\omega \leq 1$  is a positive factor that scales the increment. The  $\kappa$  superscripts denote element-local quantities.  $\mathcal{J}_{\min}^\kappa$  is the minimum Jacobian determinant for cell  $\kappa$ . The compressible Navier-Stokes system is assumed (Section 2.2).

---

**Input:**  $(y, \sigma, u)_i$

converged  $\leftarrow$  False

**while** not converged **do**

  Compute  $\Delta(y, \sigma, u)_i$

$\omega \leftarrow 1, \omega_a \leftarrow 0, \omega_b \leftarrow 1$

$(y, \sigma, u)^* \leftarrow (y, \sigma, u)_i$

$N_{\text{search}} \leftarrow 5$

**for**  $k \leftarrow 0$  to  $N_{\text{search}}$  **do**

**if**  $k > 0$  **then**

$\omega \leftarrow (\omega_a + \omega_b)/2$

**end if**

$(y, \sigma, u)_{i+1} \leftarrow (y, \sigma, u)_i + \omega \Delta(y, \sigma, u)_i$

$F_\rho \leftarrow \max_\Omega \{|\rho_{i+1} - \rho_i|/\rho_i\}$

$F_P \leftarrow \max_\Omega \{|P(y_{i+1}) - P(y_i)|/P(y_i)\}$

**if**  $\|e_h(y, \sigma, u)_{i+1}\| / \|e_h(y, \sigma, u)^*\| < 1$  and  $F_\rho \leq f$  and  $F_P \leq f$  **then**

**if**  $\omega = 1$  **then**

**break**

**end if**

$(y, \sigma, u)^* \leftarrow (y, \sigma, u)_{i+1}$

$\omega_a \leftarrow \omega$

**else**

$\omega_b \leftarrow \omega$

**end if**

**if**  $\omega_a = 0$  and  $N_{\text{search}} = 5$  **then**

$N_{\text{search}} \leftarrow N_{\text{search}} + 10$

$\triangleright$  Could not reduce  $\|e_h(y, \sigma, u)\|$ ; increase  $N_{\text{search}}$

**end if**

**end for**

$(y, \sigma, u)_{i+1} \leftarrow (y, \sigma, u)^*$

  converged  $\leftarrow$  True

**for** each element  $\kappa$  **do**

**if**  $\mathcal{J}_{\min}^{\kappa, i+1} < \mathcal{J}_b^\kappa$  **then**

      converged  $\leftarrow$  False

$\lambda_{\Delta u}^\kappa \leftarrow 10\lambda_{\Delta u}^\kappa, \lambda_b^\kappa \leftarrow 10\lambda_b^\kappa, \lambda_1^\kappa \leftarrow 100\lambda_1^\kappa$

$\mathcal{J}_b^\kappa \leftarrow 10\mathcal{J}_{\min}^{\kappa, i}$

**end if**

**end for**

**end while**

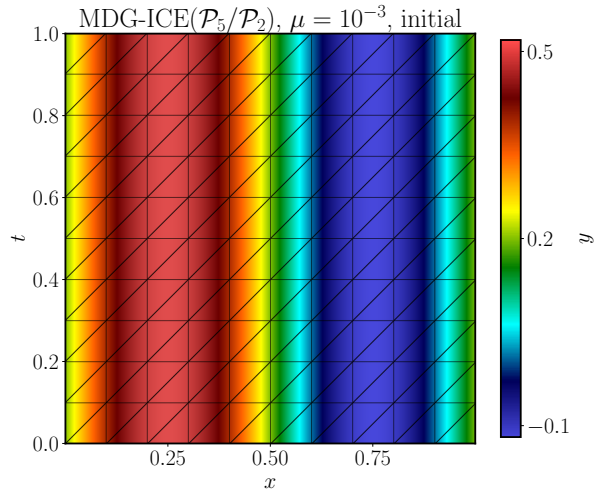
---

$$y(x, t = 0) = \frac{1}{2\pi t_s} \sin(2\pi x) + y_\infty, \quad (5.1)$$

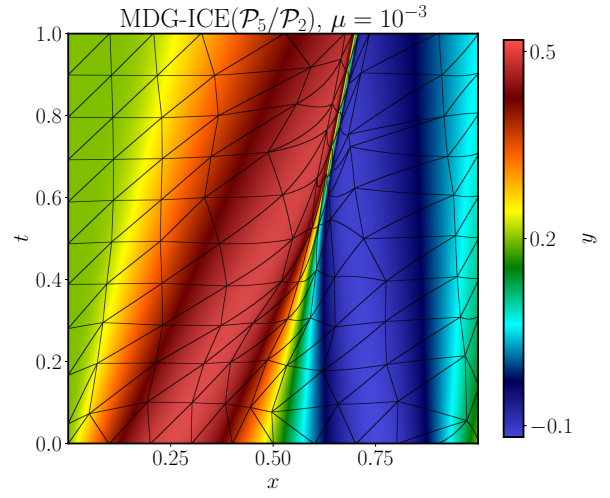
where  $t_s = 0.5$  is the time of shock formation and  $y_\infty = 0.2$  is the freestream velocity. The computational domain is  $\Omega = [0, 1] \times [0, 1]$ . Inflow and outflow boundary conditions are applied at the left and right boundaries, respectively. The solution is initialized by extruding the initial condition (5.1) in the temporal direction. We employ continuation in  $\mu$ , i.e., a series of problems is solved in which  $\mu$  is successively decreased, with the final solution of a given problem used as the initial condition of the subsequent one. In previous work [2], subparametric MDG-ICE( $\mathcal{P}_5/\mathcal{P}_1$ ) solutions were computed, also with  $\mu$  continuation. Specifically, viscosities of  $\mu = 10^{-3}$ ,  $\mu = 5 \times 10^{-4}$ , and  $\mu = 10^{-4}$  were considered. The initial grid consisted of 200 linear triangular elements obtained by splitting each element of a uniform  $10 \times 10$  quadrilateral mesh into two triangles, resulting in a regular topology. Here, we compute subparametric MDG-ICE( $\mathcal{P}_5/\mathcal{P}_2$ ) solutions for a more challenging series of viscosities:  $\mu = 10^{-3}$ ,  $\mu = 10^{-4}$ , and  $\mu = 10^{-5}$ . We employ two different starting grids: the first is the same as in [2] (i.e., a regular grid with 200 triangular elements), while the second is an irregular grid with 242 triangular elements. A key difference with [2] is that the elements are of quadratic geometric order, significantly increasing the difficulty of achieving solution convergence while maintaining a valid grid.

#### 5.1.1. Initial mesh topology: Regular

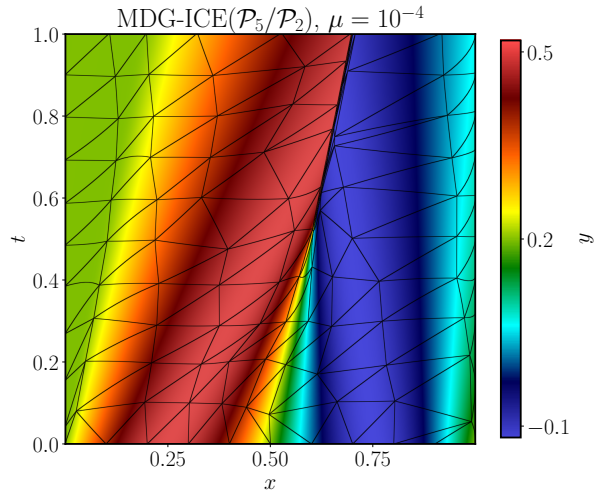
Figure 5.1a presents the space-time initial condition and final solutions for  $\mu = 10^{-3}$ ,  $\mu = 10^{-4}$ , and  $\mu = 10^{-5}$ , with the corresponding grids superimposed. Figure 5.2 shows the corresponding one-dimensional profiles at  $t = 0.025$  and  $t = 0.975$ . MDG-ICE automatically adjusts the grid geometry to resolve the viscous shock as a sharp yet smooth profile without relying on artificial stabilization or mesh-topology modification. As the viscosity is decreased, the viscous shock becomes thinner and the aspect ratios of the nearby elements are increased via anisotropic space-time  $r$ -adaptivity. The solutions are free from spurious oscillations. The anisotropic, locally adaptive penalty technique described in Section (4) enable excellent resolution of the thin viscous shock while maintaining grid validity.



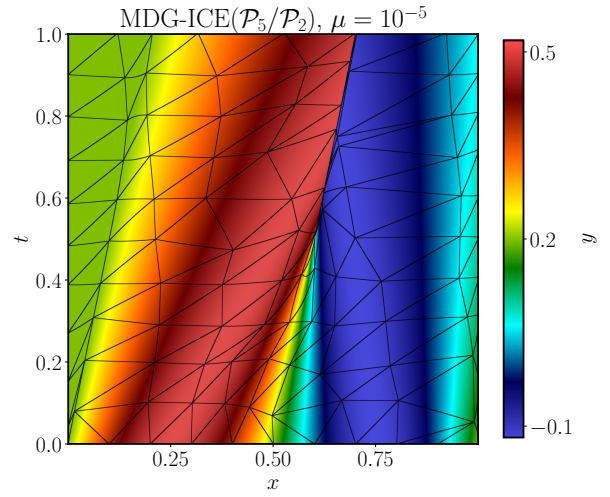
(a) Initial condition.



(b)  $\mu = 10^{-3}$  solution.

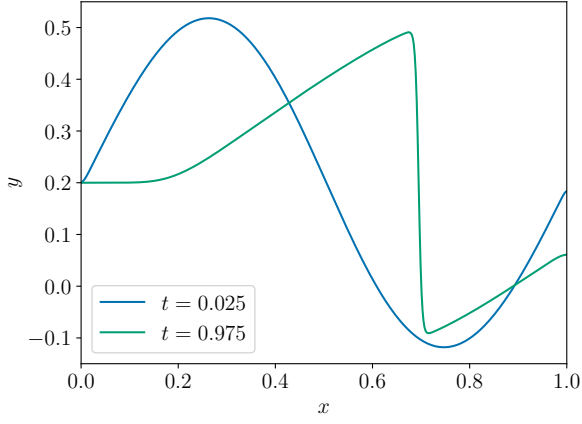


(c)  $\mu = 10^{-4}$  solution.

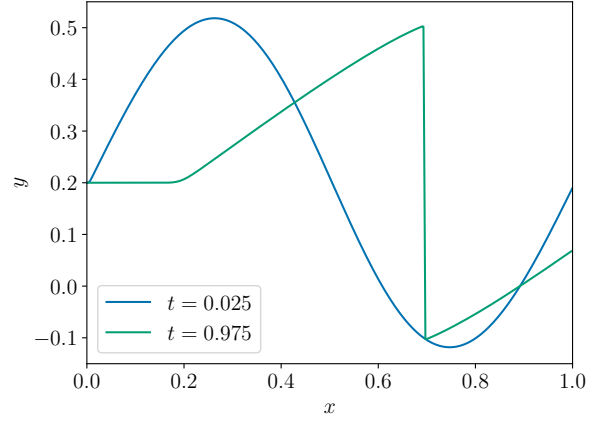


(d)  $\mu = 10^{-5}$  solution.

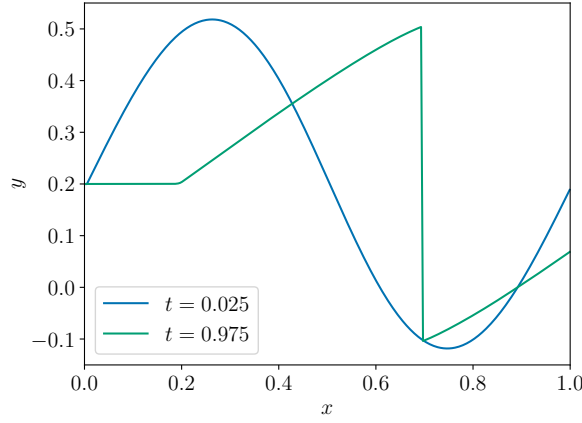
Figure 5.1: The space-time Burgers initial condition and final solutions for  $\mu = 10^{-3}$ ,  $\mu = 10^{-4}$ , and  $\mu = 10^{-5}$ , with the corresponding grids superimposed. The initial grid consists of 200 triangular elements of quadratic geometric order with a regular topology. The initial condition is given in Equation (5.1).



(a)  $\mu = 10^{-3}$  solution.



(b)  $\mu = 10^{-4}$  solution.



(c)  $\mu = 10^{-5}$  solution.

Figure 5.2: One-dimensional profiles at  $t = 0.025$  and  $t = 0.975$  for  $\mu = 10^{-3}$ ,  $\mu = 10^{-4}$ , and  $\mu = 10^{-5}$  for space-time Burgers viscous shock formation. The initial grid consists of 200 triangular elements of quadratic geometric order with a regular topology. The initial condition is given in Equation (5.1).

The nonlinear convergence history is given in Figure 5.3. The initial residual magnitudes for the  $\mu = 10^{-4}$  and  $\mu = 10^{-5}$  simulations are relatively small since the solver is restarted from the corresponding higher-viscosity solution.

#### 5.1.2. Initial mesh topology: Irregular

The initial 242-element irregular grid, along with the initial condition, is displayed in Figure 5.4a. The final solutions and grids for  $\mu = 10^{-3}$ ,  $\mu = 10^{-4}$ , and  $\mu = 10^{-5}$  are given in Figures 5.4b, 5.4c, and 5.4d, respectively. Figure 5.5 presents the corresponding one-dimensional profiles at  $t = 0.025$  and  $t = 0.975$ . Similar to the regular-topology case, MDG-ICE automatically modifies the location, size, and orientation of elements to resolve the viscous shock via anisotropic space-time  $r$ -adaptivity. Additional grid adjustments are introduced accordingly as the viscosity is decreased and the shock becomes more difficult to resolve. The final solutions are well-resolved and free from spurious oscillations. The nonlinear convergence history is displayed in Figure 5.6.

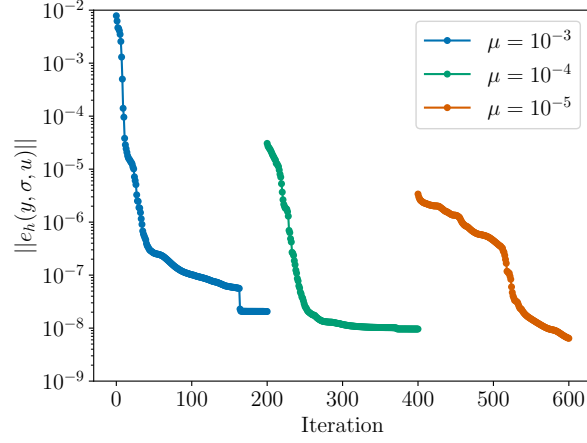


Figure 5.3: Nonlinear convergence history for space-time Burgers viscous shock formation. The initial grid consists of 200 triangular elements of quadratic geometric order with a regular topology. The initial condition is given in Equation (5.1).

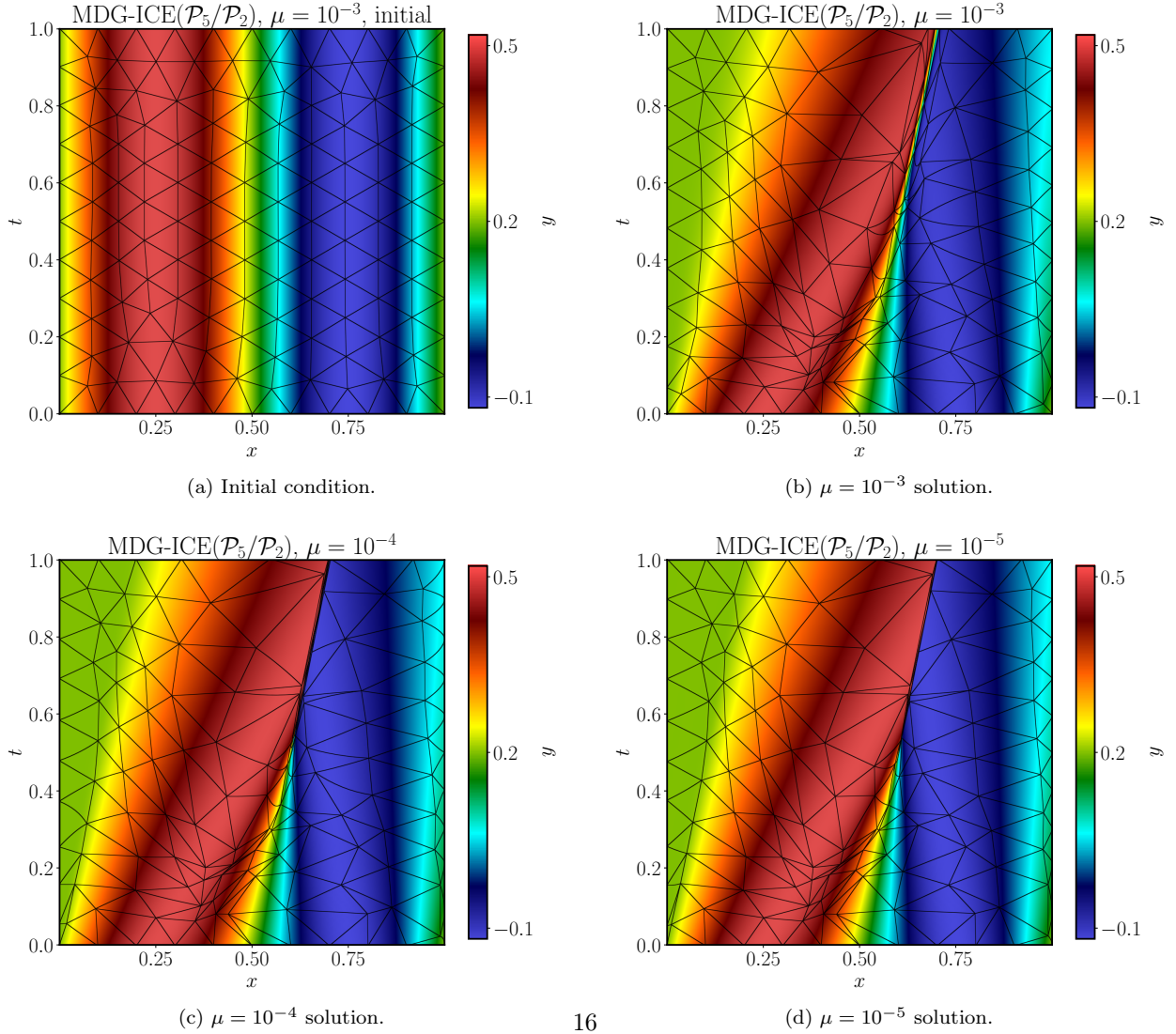


Figure 5.4: The space-time Burgers initial condition and final solutions for  $\mu = 10^{-3}$ ,  $\mu = 10^{-4}$ , and  $\mu = 10^{-5}$ , with the corresponding grids superimposed. The initial grid consists of 242 triangular elements of quadratic geometric order with an irregular topology. The initial condition is given in Equation (5.1).



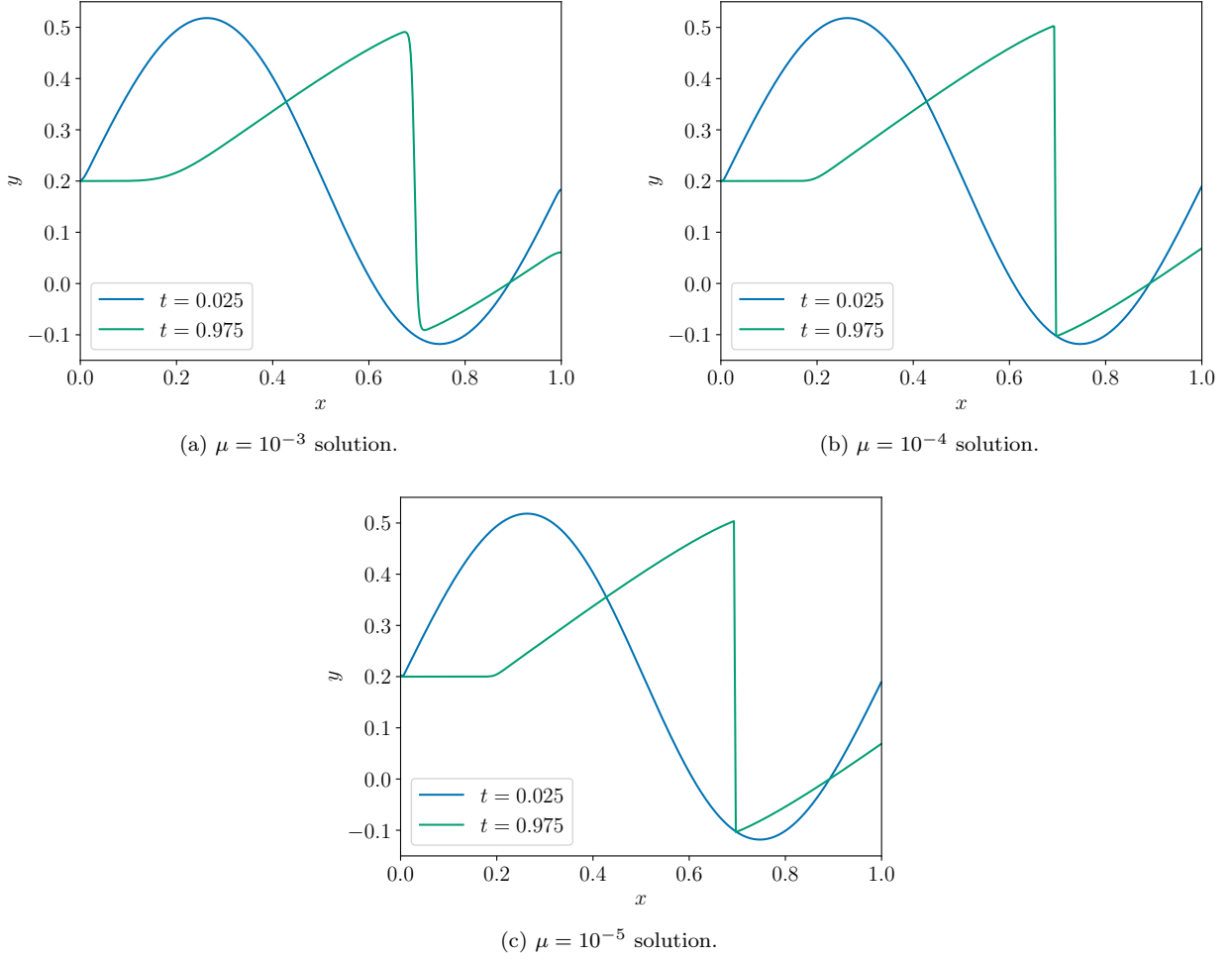


Figure 5.5: One-dimensional profiles at  $t = 0.025$  and  $t = 0.975$  for  $\mu = 10^{-3}$ ,  $\mu = 10^{-4}$ , and  $\mu = 10^{-5}$  for space-time Burgers viscous shock formation. The initial grid consists of 242 triangular elements of quadratic geometric order with an irregular topology. The initial condition is given in Equation (5.1).

## 5.2. Mach 17.6 flow over two-dimensional cylinder

Next, we compute steady hypersonic viscous flow over a circular half-cylinder in two spatial dimensions. The freestream Mach number and Reynolds number (based on the cylinder radius) are 17.6 and 376,930, respectively. This problem is a common benchmark case for evaluating the ability of numerical techniques to predict hypersonic flows. With conventional finite volume techniques [17, 18], significant asymmetries in the surface heat-flux profile were observed on both regular and irregular simplicial grids. Note that fairly symmetric heating results have been obtained on simplicial grids with DG schemes equipped with smooth artificial viscosity [40, 7]. In this work, we aim to use the proposed MDG-ICE formulation to achieve symmetric solutions without artificial dissipation. We employ two different starting grids: the first is a regular grid with 392 elements, while the second is an irregular grid with 526 elements. Freestream conditions are imposed at the inflow boundary, defined as the ellipse  $(x/6)^2 + (y/3)^2 = 1$ . Extrapolation is employed at the outflow boundary, and the cylinder boundary, a half-circle of unit radius, is an isothermal no-slip wall with temperature  $T_{\text{wall}} = 2.5T_{\infty}$ .

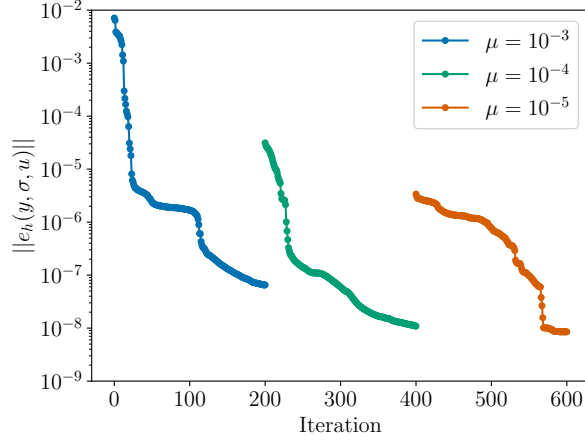


Figure 5.6: Nonlinear convergence history for space-time Burgers viscous shock formation. The initial grid consists of 242 triangular elements of quadratic geometric order with an irregular topology. The initial condition is given in Equation (5.1).

#### 5.2.1. Initial mesh topology: Regular

We employ continuation in both the Mach number and the Reynolds number, starting with an isoparametric MDG-ICE( $\mathcal{P}_4$ ) solution corresponding to  $\text{Ma} = 5, \text{Re} = 500$ . This MDG-ICE solution is initialized with a conventional DG solution stabilized with elementwise-constant artificial viscosity of the form described in [41]. Keeping  $\text{Re}$  fixed at 500, the Mach number is consecutively increased by increments of one until the target value of 17.6 is reached. These intermediate solutions are not fully converged to a stationary point. Note that the  $\text{Ma} = 17.6, \text{Re} = 500$  solution was computed in previous work [42] prior to development of the adaptive, elementwise regularization strategy (Section 4.2) and the increment-limiting procedure (Section 4.3); cell degeneration was treated then using a standard cell-collapse algorithm [29], resulting in a total of 388 elements. The 388-element mesh and temperature field for this  $\text{Ma} = 17.6, \text{Re} = 500$  solution are presented in Figure 5.7. The elements in the vicinity of the shock are anisotropic yet still valid. The MDG-ICE solution is free from oscillations even in the absence of artificial dissipation.

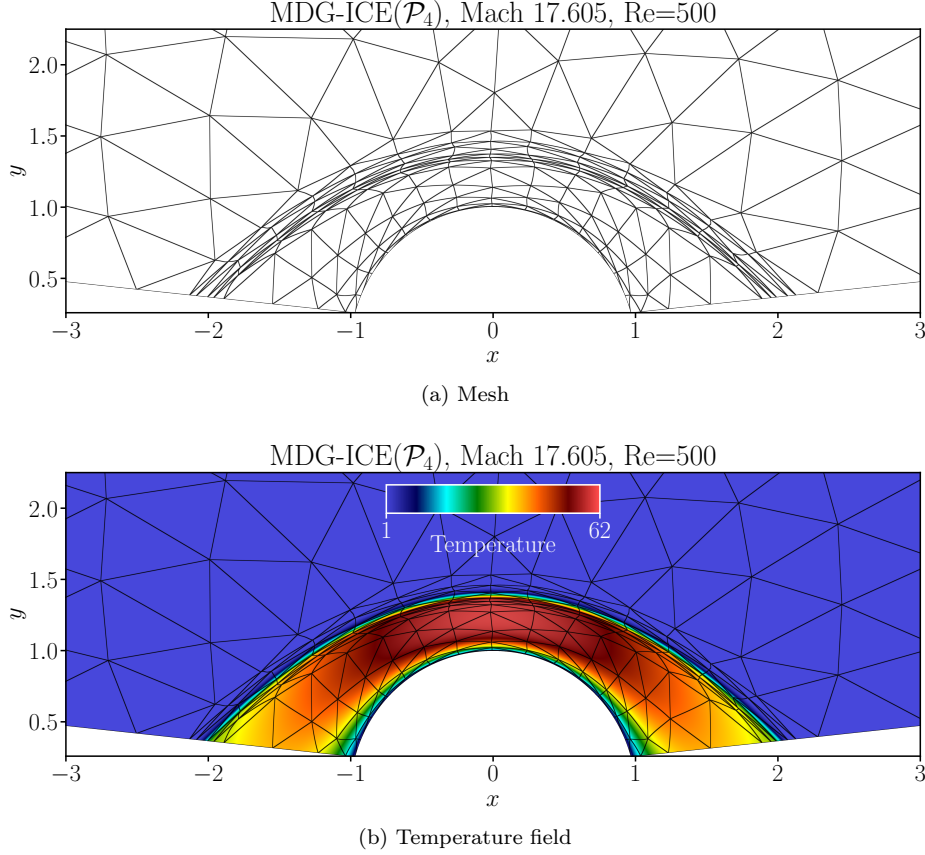


Figure 5.7: The MDG-ICE solution computed using 388  $\mathcal{P}_4$  isoparametric triangle elements for two-dimensional Mach 17.6 flow over a cylinder at  $\text{Re} = 500$ . The initial grid has a regular topology.

The Reynolds number is then consecutively increased by factors of approximately two until the target value of 376,930 is reached. At this Reynolds number, we increase the polynomial degrees of  $Y_h$  and  $\Sigma_h$  from four to five in order to eliminate slight asymmetries in the surface heat-flux profile, as will be shown later in this section. The final mesh and temperature, Mach, and pressure fields are given in Figure 5.8. Considerable jumps in temperature and pressure are observed. MDG-ICE automatically adjusts the grid geometry in order to resolve the viscous shock and boundary layer, which become sharper as the Reynolds number is increased. Highly anisotropic elements are observed at the shock and in the boundary layer, yet grid validity is maintained as a result of the anisotropic Laplacian-type regularization and the adaptive, elementwise regularization strategy. The solution is well-resolved and free from spurious artifacts. Despite the initially regular nature of the mesh, there is undoubtedly very strong misalignment between the grid and the shock and boundary layer. Figure 5.9 displays the nonlinear convergence history for the subparametric MDG-ICE( $\mathcal{P}_5/\mathcal{P}_4$ ) solution. The residual starts at a relatively small value since the simulation is restarted from an isoparametric MDG-ICE( $\mathcal{P}_4$ ) solution. Future work will focus on incorporating stabilization mechanisms (at least during early/intermediate iterations) and/or space-time marching in order to accelerate convergence and circumvent the need for continuation in Mach number and Reynolds number, which itself can be considered akin to (global) artificial dissipation. Nevertheless, this demonstrates how MDG-ICE can be naturally employed for parametric studies in which the flow conditions are varied; other grid adaptation strategies may need to incorporate coarsening techniques to maintain efficiently refined grids.

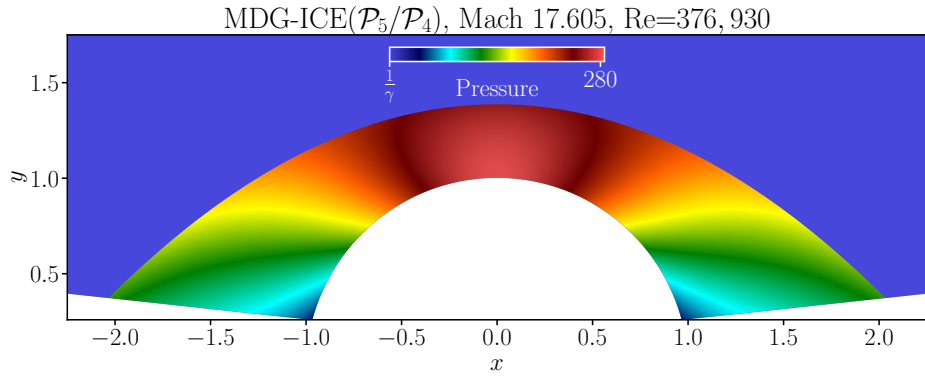
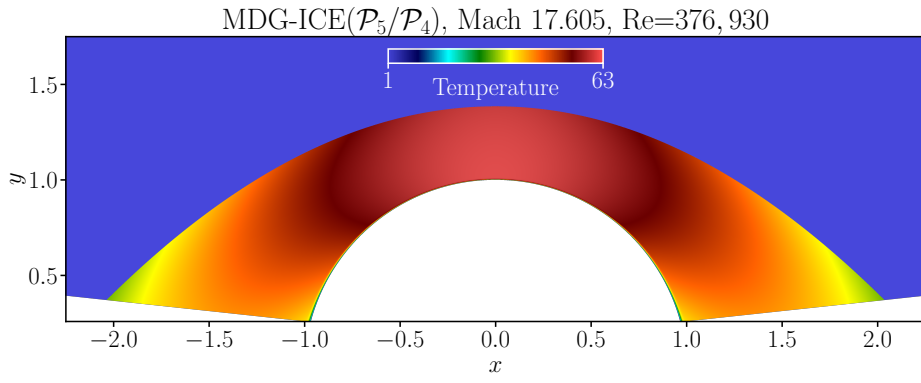
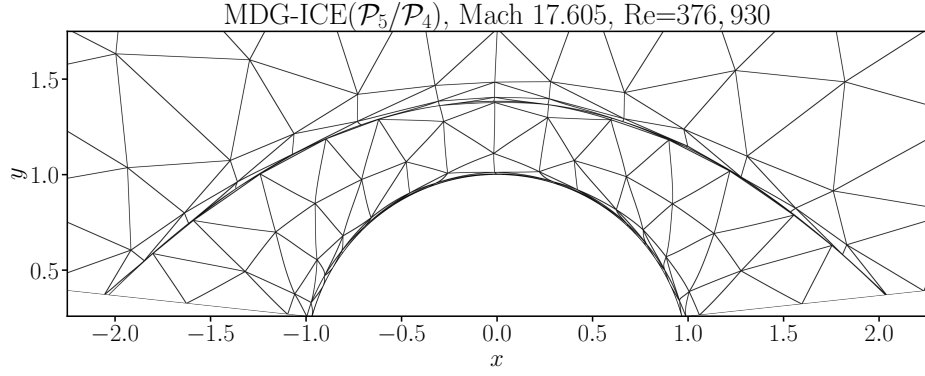


Figure 5.8: The MDG-ICE solution computed using 388 subparametric  $\mathcal{P}_5/\mathcal{P}_4$  triangle elements for two-dimensional Mach 17.6 flow over a cylinder at  $\text{Re} = 376,930$ . The initial grid has a regular topology.

Figure 5.10 presents the isoparametric MDG-ICE( $\mathcal{P}_4$ ) and subparametric MDG-ICE( $\mathcal{P}_5/\mathcal{P}_4$ ) predictions of the pressure coefficient and Stanton number, defined as

$$C_p = \frac{P - P_\infty}{\frac{1}{2}\rho_\infty v_\infty^2}$$

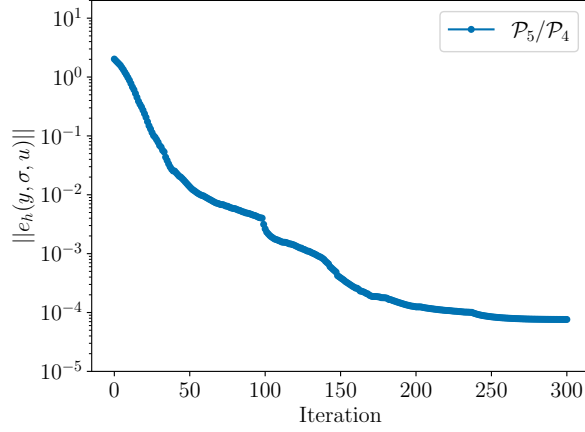


Figure 5.9: Nonlinear convergence history for the subparametric MDG-ICE( $\mathcal{P}_5/\mathcal{P}_4$ ) solution to Mach 17.6 flow over a two-dimensional cylinder. The initial grid has a regular topology.

and

$$C_h = \frac{q_n}{c_p \rho_\infty v_\infty (T_{t,\infty} - T_{\text{wall}})},$$

respectively, where  $q_n$  is the normal heat flux and  $T_t$  is the stagnation temperature. The pressure profiles for both MDG-ICE solutions are highly symmetric, but the heat-flux profile for the isoparametric MDG-ICE( $\mathcal{P}_4$ ) solution exhibits a slight nonphysical cusp at the stagnation point. Nevertheless, this cusp is eliminated with  $p$ -refinement. The stagnation-point Stanton number in the MDG-ICE( $\mathcal{P}_5/\mathcal{P}_4$ ) solution is approximately 0.0077. Note that there exists some variation in the stagnation-point Stanton number reported in the literature; for example, 0.0085 in [18], 0.0076 in [43], and 0.0082 in [40].

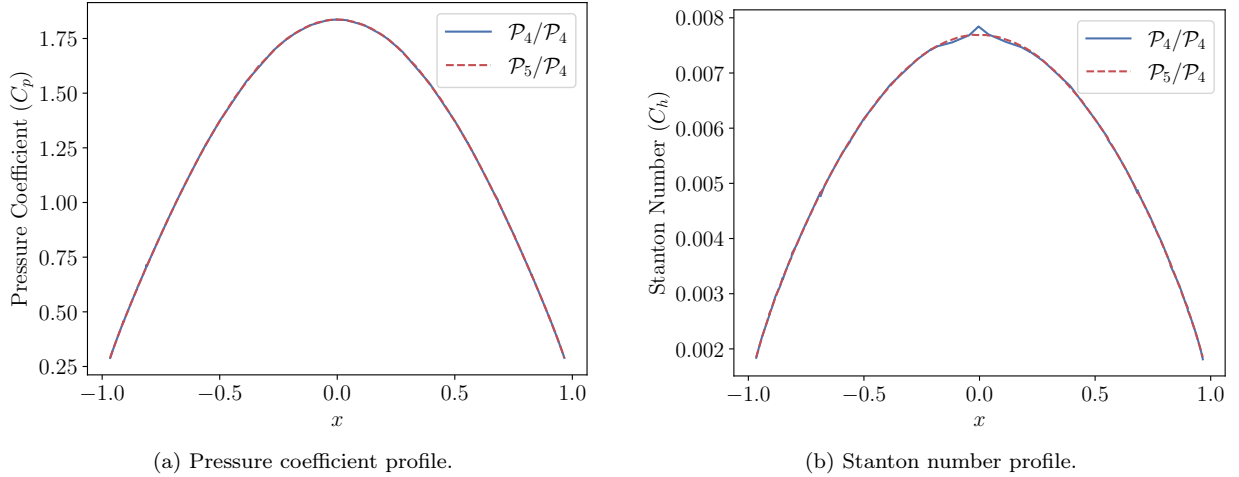


Figure 5.10: Surface profiles of pressure coefficient and Stanton number for the MDG-ICE solution computed using 388  $\mathcal{P}_5/\mathcal{P}_4$  triangle elements for two-dimensional Mach 17.6 flow over a cylinder at  $\text{Re} = 376,930$ . The initial grid has a regular topology.

### 5.2.2. Initial mesh topology: Irregular

Continuation in the Mach and Reynolds numbers is once again employed, starting with  $\text{Ma} = 5$ ,  $\text{Re} = 100$ . The 526-element mesh and temperature field for an intermediate MDG-ICE solution at  $\text{Ma} = 5$ ,  $\text{Re} = 100$

are presented in Figure 5.11. The temperature field is smooth. At this low Reynolds number, only slight grid repositioning is required to resolve the flow.

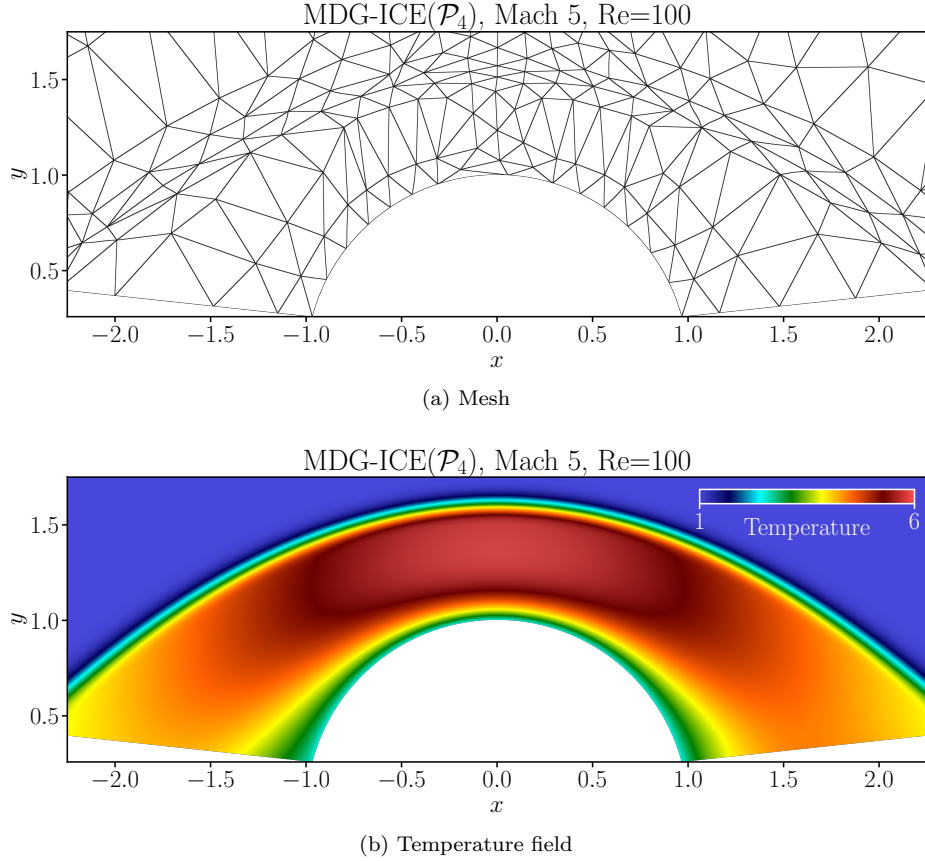


Figure 5.11: The MDG-ICE solution computed using 526  $\mathcal{P}_4$  isoparametric triangle elements for for two-dimensional Mach 17.6 flow over a cylinder at  $\text{Re} = 100$ . The initial grid has an irregular topology.

Global  $p$ -refinement of the state and auxiliary-variable approximations is again employed. The final subparametric MDG-ICE( $\mathcal{P}_5/\mathcal{P}_4$ ) solution at  $\text{Ma} = 17.6, \text{Re} = 376,930$  is given in Figure 5.12. The long, thin elements oriented orthogonal to the shock are a direct consequence of two main factors associated with the initially irregular nature of the grid: (a) moreso than in the regular case, incrementing the Mach and Reynolds numbers (in the absence of additional stabilization) causes transient artifacts to appear upstream of the shock, which then induce appreciable grid motion; (b) the compression of the grid at the shock and boundary layer is less likely to pull in outlying elements accordingly than in the regular case. Note that starting with intermediate Reynolds numbers,  $\alpha$  is set to zero in order to alleviate excessive stiffening of the anisotropic, shock-orthogonal elements due to the Laplacian regularization (4.7). Although it is not clear how detrimental this type of element may be in more complex configurations (if at all), the formation of such elements can be mitigated by, as previously discussed, the use of artificial dissipation during intermediate iterations and/or metric-based remeshing. Nevertheless, the thin viscous structures remain sharp and free from spurious oscillations.

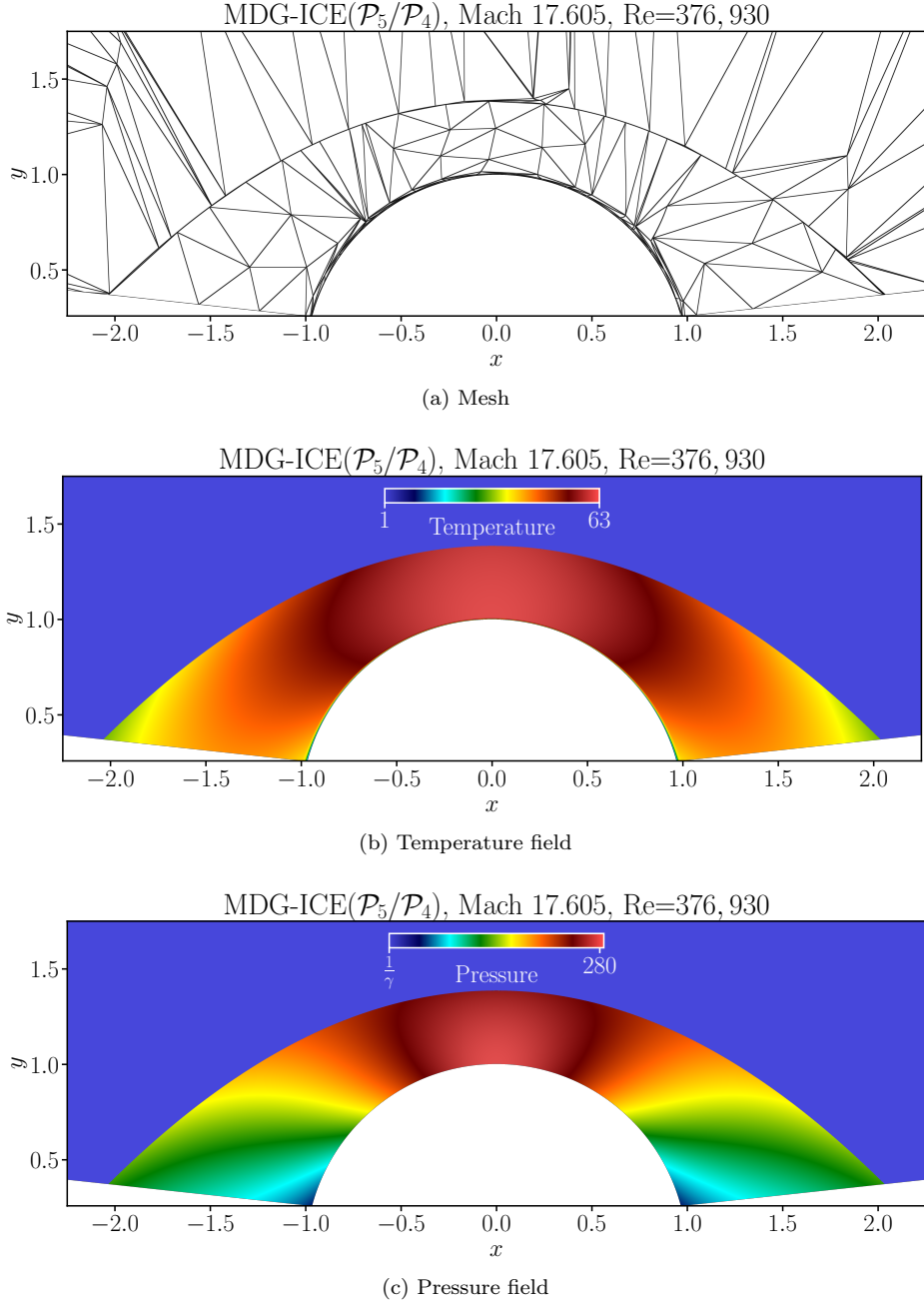


Figure 5.12: The MDG-ICE solution computed using 526  $\mathcal{P}_5/\mathcal{P}_4$  subparametric triangle elements for two-dimensional Mach 17.6 flow over a cylinder at  $\text{Re} = 376,930$ . The initial grid has an irregular topology.

Figure 5.9 displays the nonlinear convergence history for the subparametric MDG-ICE( $\mathcal{P}_5/\mathcal{P}_4$ ) solution. The initial residual is already low since the simulation is restarted from an isoparametric MDG-ICE( $\mathcal{P}_4$ ) solution.

Figure 5.14 presents the surface profiles of pressure coefficient and Stanton number for the subparametric MDG-ICE( $\mathcal{P}_5/\mathcal{P}_4$ ) solution. The stagnation-point Stanton number is approximately 0.0077. Despite the evidently asymmetric grid and extremely strong grid-shock misalignment, the surface profiles are highly



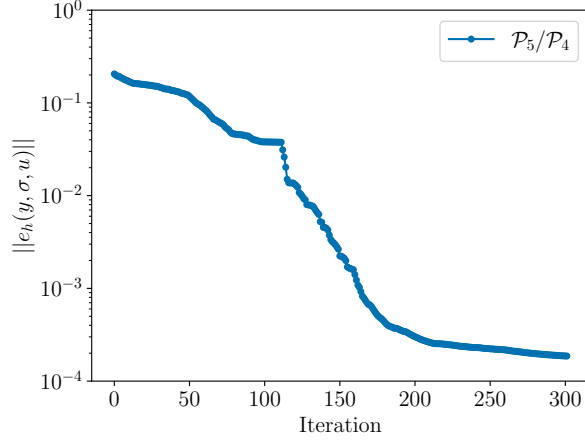


Figure 5.13: Nonlinear convergence history for the subparametric MDG-ICE( $\mathcal{P}_5/\mathcal{P}_4$ ) solution to Mach 17.6 flow over a two-dimensional cylinder. The initial grid has an irregular topology.

symmetric and agree well with those in Figure (5.10).

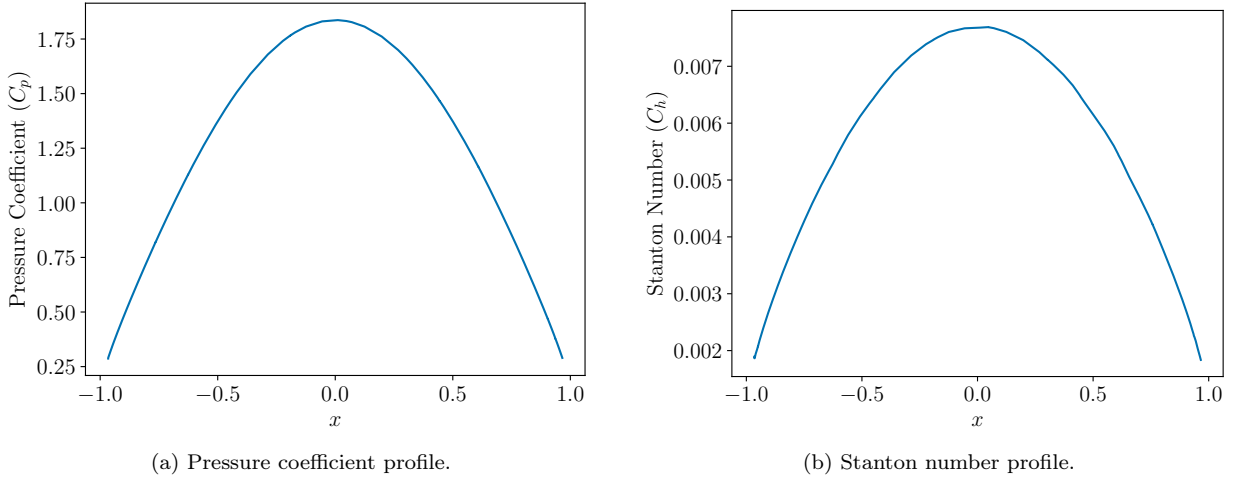


Figure 5.14: Surface profiles of pressure coefficient and Stanton number obtained with the MDG-ICE solution computed using 526  $\mathcal{P}_5/\mathcal{P}_4$  subparametric triangle elements for two-dimensional Mach 17.6 flow over a cylinder at  $\text{Re} = 376,930$ . The initial grid has an irregular topology.

### 5.3. Mach 17.6 flow over three-dimensional cylinder

This test case is the three-dimensional version of the previous configuration. The consideration of three spatial dimensions allows for the emergence of instabilities and asymmetries that are naturally suppressed in the two-dimensional case. In particular, it is with a three-dimensional domain that nonphysical artifacts in the heat-flux profiles obtained with finite volume schemes are most prominent [18, 17]. The two-dimensional domain is extruded one layer of cells in the homogeneous direction by two (nondimensional) units. Slip conditions are applied at the symmetry boundaries. Unlike in the previous subsection, the inflow boundary is defined as the circle  $x^2 + y^2 = 6.5^2$ . The reason for this modification is that as the Mach number is increased during the continuation strategy, spurious transients appear upstream of the shock and interact with the boundary, causing noticeable instabilities that can be dampened by positioning the inflow boundary far away from the shock. Although also present in the two-dimensional simulations, these instabilities are

exacerbated in the three-dimensional setting. Again, the use of artificial dissipation would likely resolve this issue. As in the two-dimensional case, we employ two different starting grids: the first is a regular grid with 3024 elements, while the second is an irregular grid with 3183 elements.

### 5.3.1. Initial mesh topology: Regular

Figure 5.15 provides a clipped, three-dimensional perspective of the initial grid. An isoparametric  $\text{DG}(\mathcal{P}_3)$  solution at  $\text{Ma} = 14, \text{Re} = 100$  is used as the initial condition for the MDG-ICE continuation with superparametric  $\mathcal{P}_3/\mathcal{P}_4$  cells. A positivity-preserving and entropy-based linear-scaling limiter [44, 45, 46] is employed to help maintain stability in the DG solution. The temperature field and initial grid for the DG solution along the  $z = 2$  symmetry plane are presented in Figure 5.16. Note the coarseness of the grid with respect to the expected high-gradient features at the target conditions. After reaching  $\text{Ma} = 17.6, \text{Re} = 376,930$ , two global  $p$ -refinements of the state and auxiliary-variable approximations are performed. The final subparametric MDG-ICE( $\mathcal{P}_5/\mathcal{P}_4$ ) solution is displayed in Figure 5.16. Just as in the two-dimensional case, the grid is automatically adapted to resolve the viscous shock and boundary layer while maintaining grid validity. Figure 5.18 zooms in on the shock layer along the stagnation line. Extremely high-aspect-ratio elements at the shock and boundary layer are observed. In particular, the cells at the shock are almost visually indistinguishable. Furthermore, in the temperature field, although the smoothness of the boundary layer can be discerned, the viscous shock resembles a truly discontinuous feature.

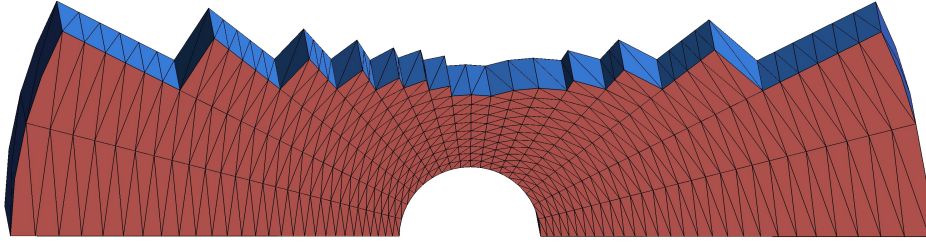


Figure 5.15: Clipped, three-dimensional perspective of the initial grid with a regular topology.

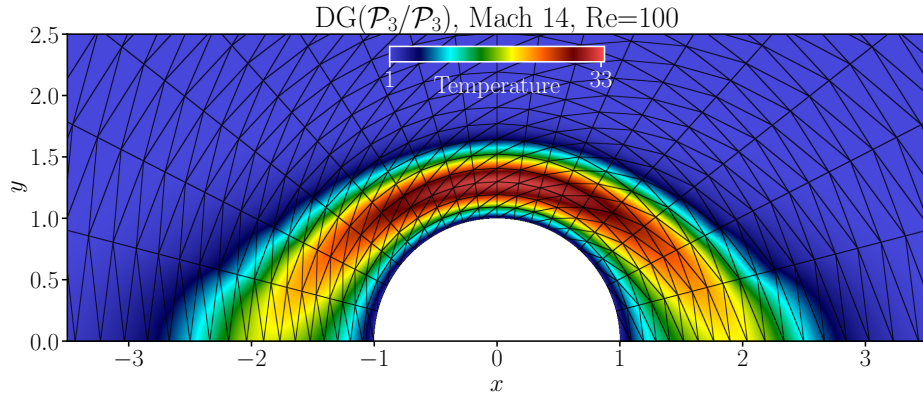
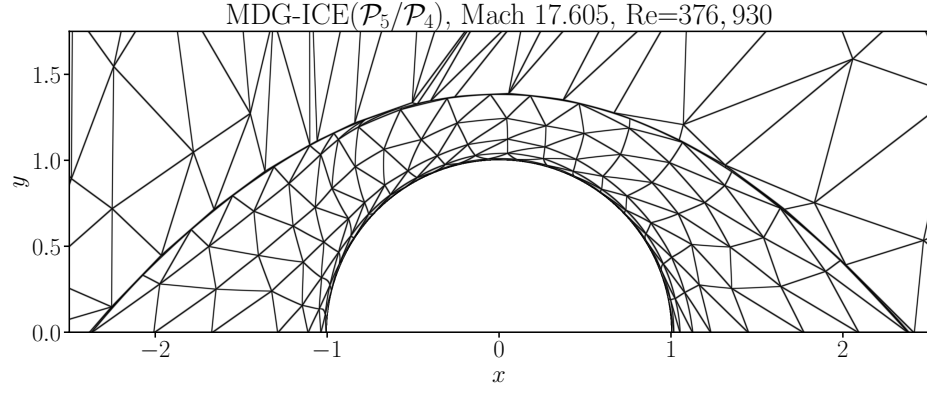
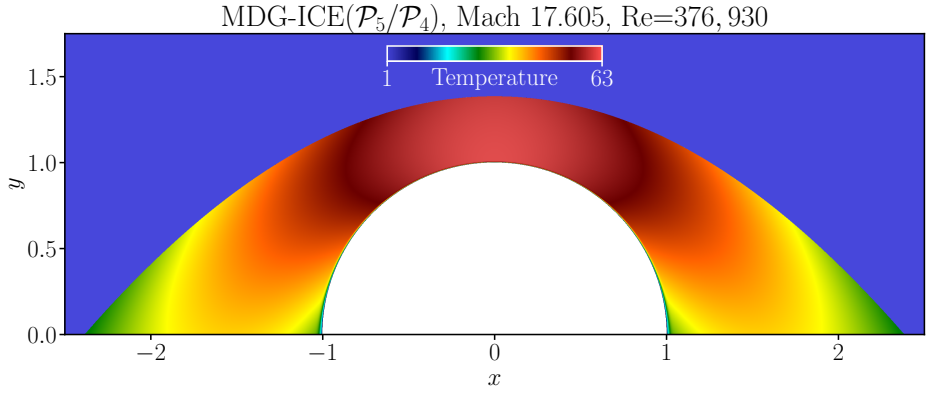


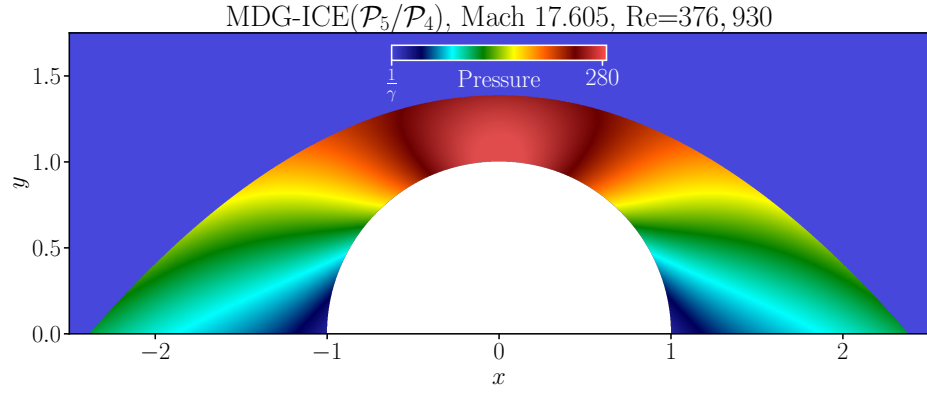
Figure 5.16: Isoparametric  $\text{DG}(\mathcal{P}_3)$  solution at  $\text{Ma} = 14, \text{Re} = 100$  on 3024 tetrahedral cells along the  $z = 2$  symmetry plane. This solution is used as the initial condition for the MDG-ICE continuation strategy. The initial grid has a regular topology.



(a) Mesh



(b) Temperature field



(c) Pressure field

Figure 5.17: The MDG-ICE solution (shown along the  $z = 2$  symmetry plane) computed using 3024  $\mathcal{P}_5/\mathcal{P}_4$  subparametric tetrahedral elements for three-dimensional Mach 17.6 flow over a cylinder at  $\text{Re} = 376,930$ . The initial grid has a regular topology.

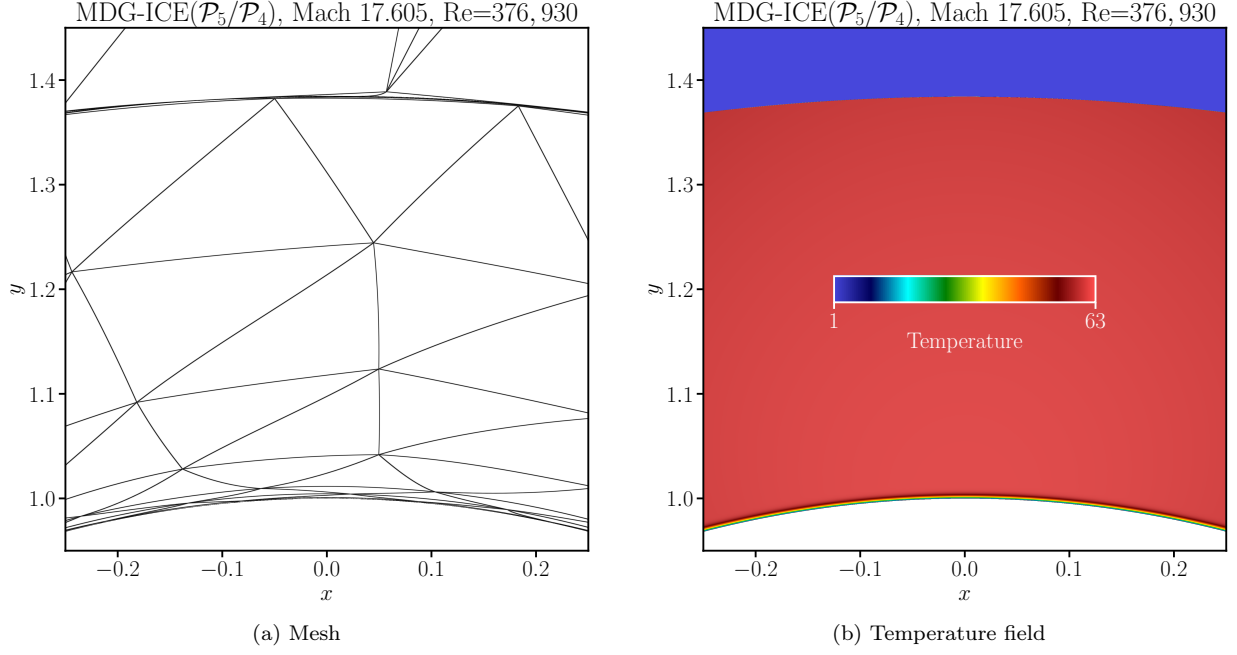


Figure 5.18: Zoomed-in view of the subparametric MDG-ICE( $\mathcal{P}_5/\mathcal{P}_4$ ) solution (shown along the  $z = 2$  symmetry plane) to three-dimensional Mach 17.6 flow over a cylinder at  $\text{Re} = 376,930$ . The initial grid has a regular topology.

The convergence history for the subparametric MDG-ICE( $\mathcal{P}_5/\mathcal{P}_4$ ) solution is given in Figure 5.19. The residual magnitude starts at a relatively small value since the solution is restarted from an isoparametric MDG-ICE( $\mathcal{P}_4$ ) calculation. Figure 5.20 shows the stagnation-line profiles of temperature and pressure. The stagnation point is located at  $y = 1$ . The stagnation-line quantities are plotted on a per-cell basis, i.e., only points within the same cell are connected. Note that it is very difficult to capture the interior of the extremely thin viscous shock using the employed line sampler, which probes the solution at discrete points. This explains why the shock is presented as a discontinuity in Figure 5.20. These results further confirm that the solution is free from spurious oscillations, despite the substantial gradient across the shock.

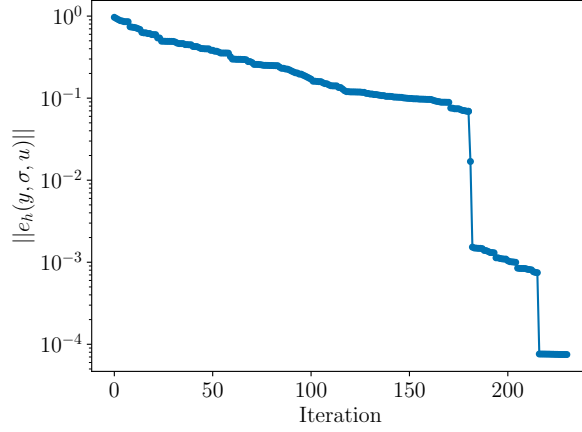


Figure 5.19: Nonlinear convergence history for the subparametric MDG-ICE( $\mathcal{P}_5/\mathcal{P}_4$ ) solution to Mach 17.6 flow over a three-dimensional cylinder. The initial grid has a regular topology.

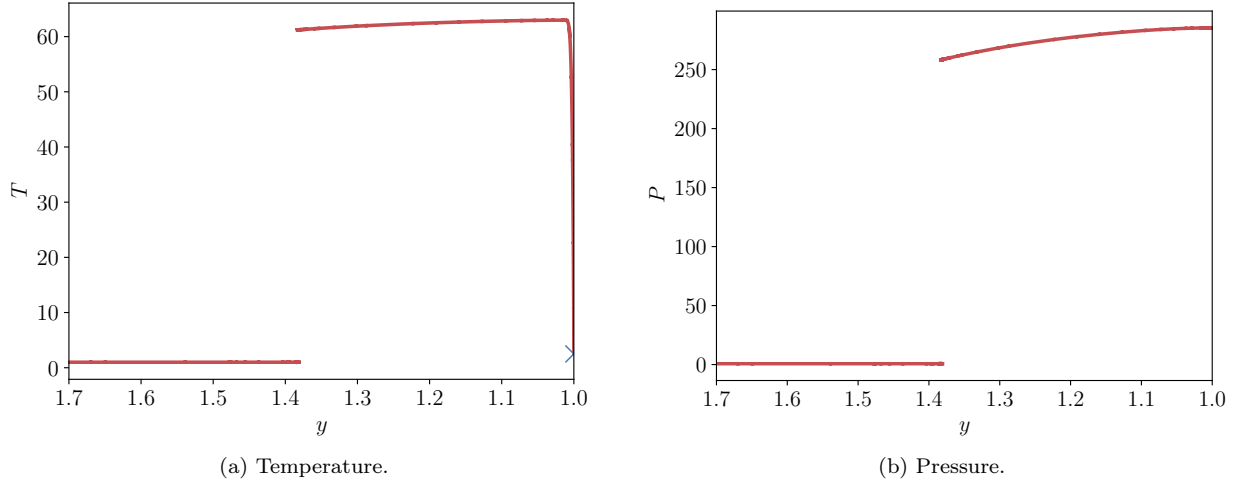


Figure 5.20: Stagnation-line profiles of temperature and pressure obtained with the MDG-ICE solution computed using 3024  $\mathcal{P}_5/\mathcal{P}_4$  subparametric tetrahedral elements for three-dimensional Mach 17.6 flow over a cylinder at  $Re = 376,930$ . The stagnation point is located at  $y = 1$ . The stagnation-line quantities are plotted on a per-cell basis, i.e., only points within the same cell are connected. The exact stagnation-point temperature,  $T = 2.5$ , is marked with the symbol  $\times$ . The initial grid has a regular topology.

Figure 5.21 gives the surface pressure and heat flux evaluated at all degrees of freedom corresponding to  $\Sigma_h$  for the subparametric MDG-ICE( $\mathcal{P}_5/\mathcal{P}_4$ ) solution. The pressure profile is essentially perfectly symmetric. Though very slight asymmetries are still present in the heat-flux profile, it is nevertheless highly symmetric. The stagnation-point Stanton number in the MDG-ICE( $\mathcal{P}_5/\mathcal{P}_4$ ) solution is approximately 0.0077.

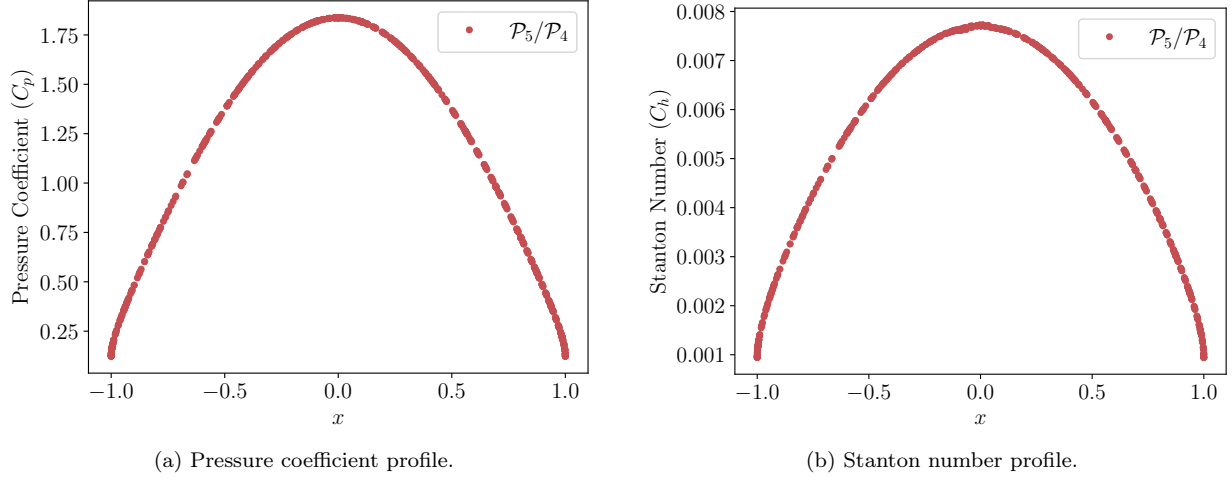


Figure 5.21: Surface profiles of pressure coefficient and Stanton number for the subparametric MDG-ICE( $\mathcal{P}_5/\mathcal{P}_4$ ) solution to three-dimensional Mach 17.6 flow over a cylinder at  $\text{Re} = 376,930$ . Pressure and heat-flux values at all auxiliary-variable degrees of freedom along the cylinder wall are shown. The initial grid has a regular topology.

### 5.3.2. Initial mesh topology: Irregular

A clipped, three-dimensional view of the initial grid is presented in Figure 5.22. In order to reduce the computational cost and memory footprint of the linear solver, the initial grid is made finer in the expected shock-layer region than near the inflow boundary. An isoparametric  $\text{DG}(\mathcal{P}_3)$  solution at  $\text{Ma} = 14, \text{Re} = 200$  is used as the initial condition for the MDG-ICE continuation with superparametric  $\mathcal{P}_3/\mathcal{P}_4$  cells. Figure 5.23 presents the temperature field and initial grid for the DG solution along the  $z = 2$  symmetry plane. Given the irregular nature of the grid, continuation in Reynolds number, especially at higher Reynolds numbers, leads to the appearance of temperature undershoots that are especially difficult to dampen in this problem in the absence of artificial dissipation. To mitigate these instabilities, we employ the alternative least-squares MDG-ICE formulation with optimal test functions [3] based on the discontinuous Petrov-Galerkin methodology by Demkowicz and Gopalakrishnan [47, 48, 49]. This formulation is found to be significantly more robust (in terms of preventing spurious undershoots/overshoots in flow quantities) than the standard MDG-ICE formulation. The anisotropic, locally adaptive penalty method described in Section 4 is incorporated in an analogous manner. Furthermore, the irregular nature of the grid induces larger grid motion in the shock layer, especially in response to spurious transients as the Reynolds number is increased, which can lead to excessively anisotropic grid interfaces along the cylinder surface. To prevent the appearance of such thin grid interfaces along the cylinder surface, we freeze the cylinder surface grid in the geometric projection operator,  $b(u)$ . Although it is not yet clear how detrimental the presence of unnecessarily high-aspect-ratio grid interfaces along a domain boundary may be in more complex configurations, the formation of such grid interfaces can be mitigated by the use of artificial dissipation (which can also alleviate the aforementioned instabilities) during intermediate iterations and/or metric-based remeshing.

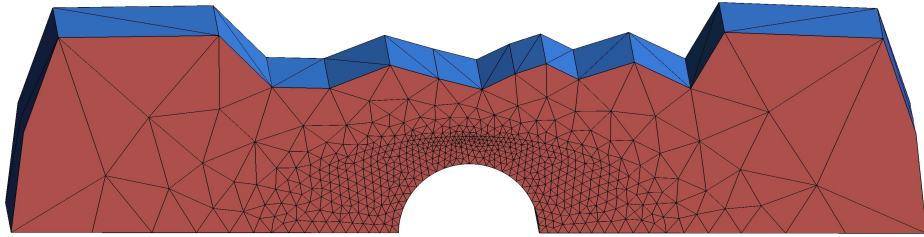


Figure 5.22: Clipped, three-dimensional perspective of the initial grid with an irregular topology.

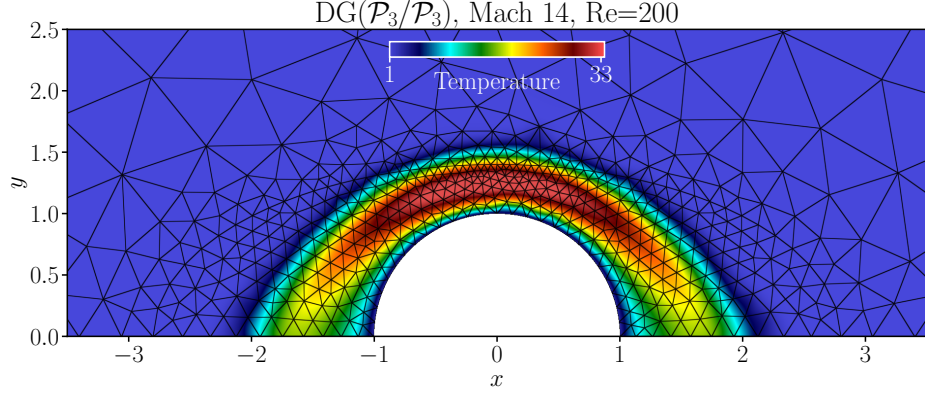


Figure 5.23: Isoparametric  $DG(\mathcal{P}_3)$  solution at  $Ma = 14, Re = 200$  on 3183 tetrahedral cells along the  $z = 2$  symmetry plane. This solution is used as the initial condition for the MDG-ICE continuation strategy. The initial grid has an irregular topology.

After reaching  $Ma = 17.6, Re = 376,930$ , two global  $p$ -refinements of the state and auxiliary-variable approximations are performed, and we revert to the standard MDG-ICE formulation since the alternative least-squares MDG-ICE formulation with optimal test functions [3] is no longer needed at this point. Figure 5.23 displays the final subparametric MDG-ICE( $\mathcal{P}_5/\mathcal{P}_4$ ) solution. The grid is ostensibly more irregular than the previous grid and, as in the two-dimensional case, features long, thin elements oriented orthogonal to the shock. Nevertheless, the shock and boundary layer remain well-resolved. Figure 5.25 zooms in on the shock layer along the stagnation line. Again, the cells at the shock are almost visually indistinguishable, and the viscous shock resembles a discontinuous feature. The solution is free from spurious oscillations.



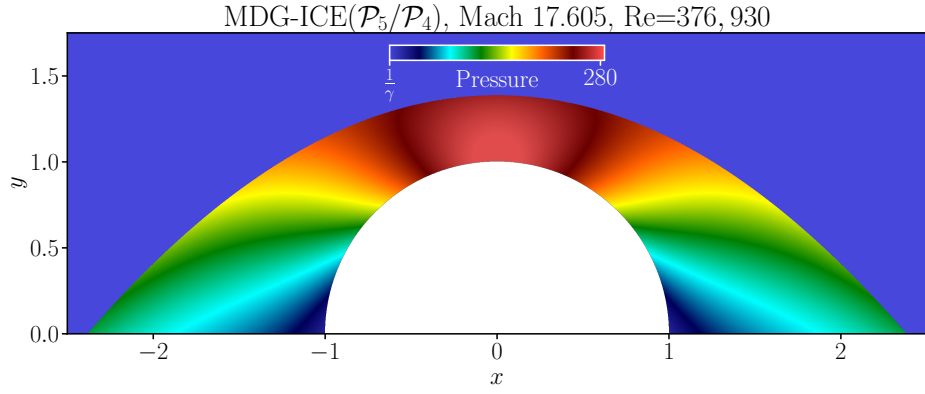
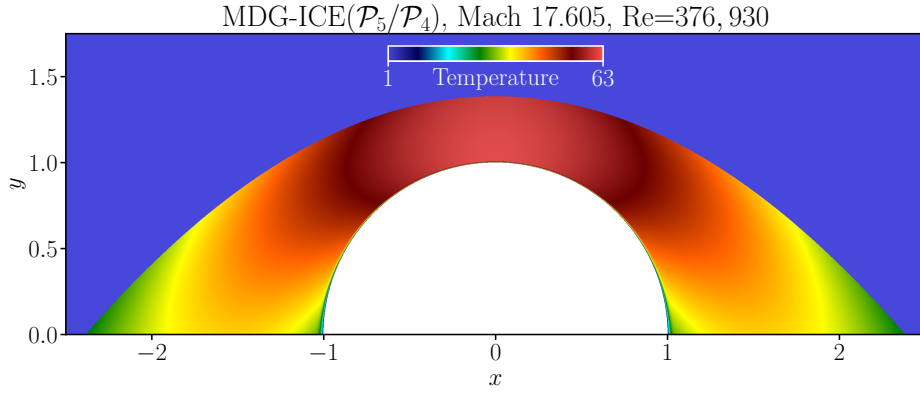
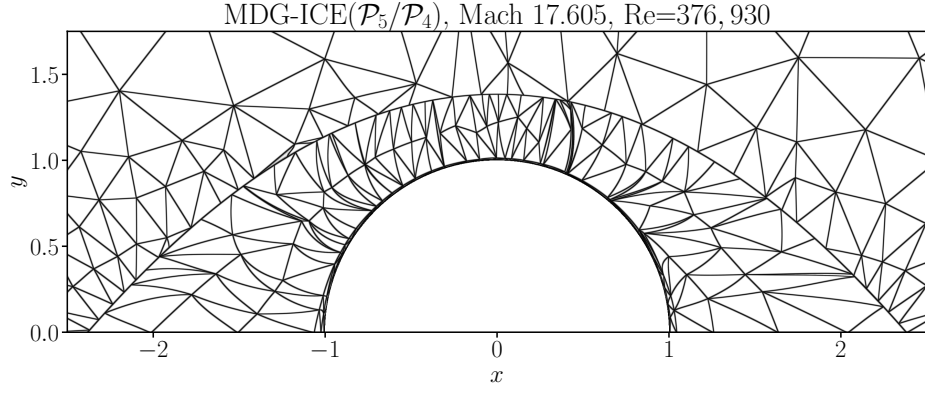


Figure 5.24: The MDG-ICE solution (shown along the  $z = 2$  symmetry plane) computed using 3183  $\mathcal{P}_5/\mathcal{P}_4$  subparametric tetrahedral elements for three-dimensional Mach 17.6 flow over a cylinder at  $\text{Re} = 376,930$ . The initial grid has an irregular topology.

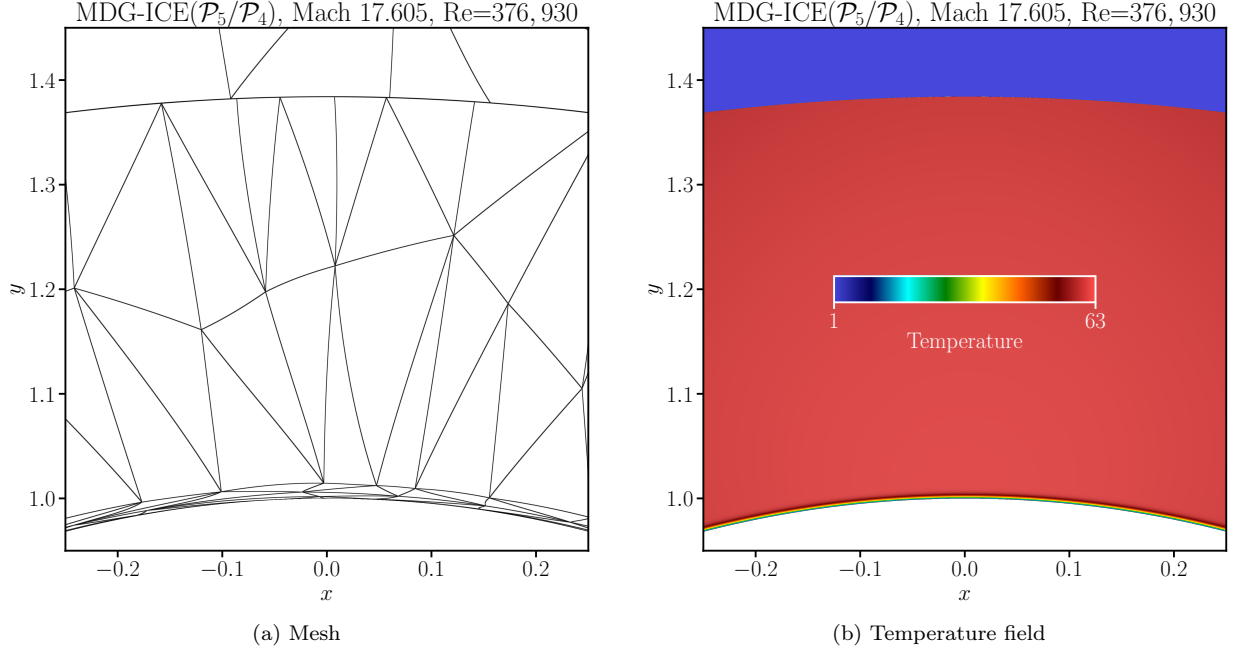


Figure 5.25: Zoomed-in view of the subparametric MDG-ICE( $\mathcal{P}_5/\mathcal{P}_4$ ) solution (shown along the  $z = 2$  symmetry plane) to three-dimensional Mach 17.6 flow over a cylinder at  $\text{Re} = 376,930$ . The initial grid has an irregular topology.

The convergence history for the subparametric MDG-ICE( $\mathcal{P}_5/\mathcal{P}_4$ ) solution is given in Figure 5.26. The residual magnitude starts at a relatively small value since the solution is restarted from an isoparametric MDG-ICE( $\mathcal{P}_4$ ) calculation.

The stagnation-line profiles of temperature and pressure are given in Figure 5.27. The stagnation point is located at  $y = 1$ . The stagnation-line quantities are plotted on a per-cell basis, which means only points within the same cell are connected. Again, it is very difficult to capture the interior of the highly anisotropic viscous shock using the employed line sampler, which probes the solution at discrete points. This explains why the shock resembles a true discontinuity in Figure 5.27. The shock and boundary layer are well-resolved.

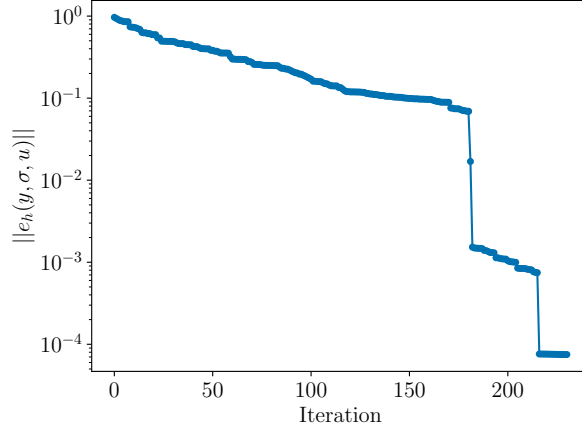


Figure 5.26: Nonlinear convergence history for the subparametric MDG-ICE( $\mathcal{P}_5/\mathcal{P}_4$ ) solution to Mach 17.6 flow over a three-dimensional cylinder. The initial grid has an irregular topology.

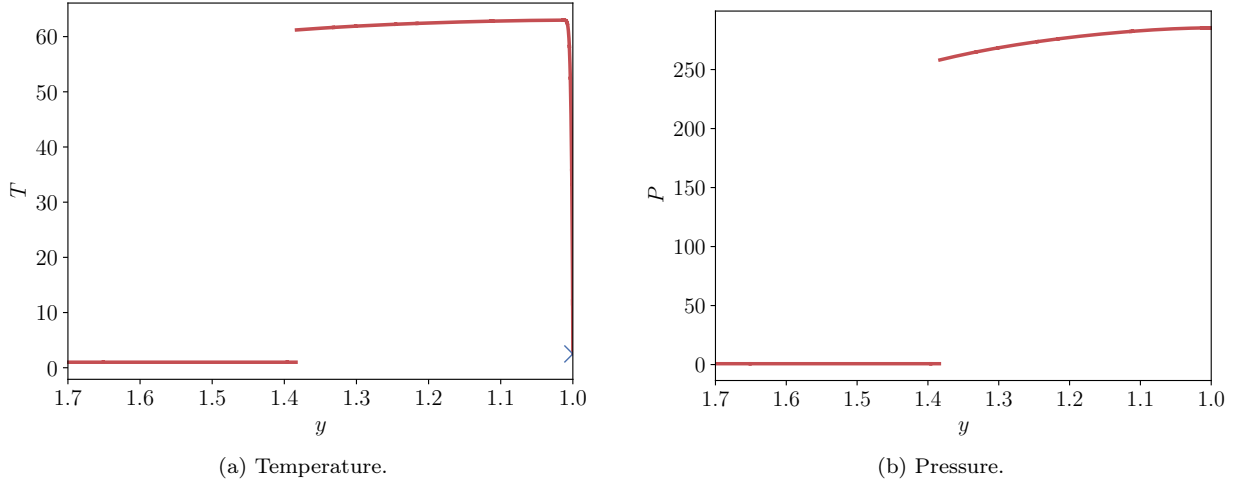


Figure 5.27: Stagnation-line profiles of temperature and pressure obtained with the MDG-ICE solution computed using 3183  $\mathcal{P}_5/\mathcal{P}_4$  subparametric tetrahedral elements for three-dimensional Mach 17.6 flow over a cylinder at  $\text{Re} = 376,930$ . The stagnation point is located at  $y = 1$ . The stagnation-line quantities are plotted on a per-cell basis, i.e., only points within the same cell are connected. The exact stagnation-point temperature,  $T = 2.5$ , is marked with the symbol  $\times$ . The initial grid has an irregular topology.

Figure 5.28 gives the surface pressure and heat flux evaluated at all degrees of freedom corresponding to  $\Sigma_h$  for the subparametric MDG-ICE( $\mathcal{P}_5/\mathcal{P}_4$ ) solution. Excellent symmetry is observed in the pressure and heat-flux profiles. Though very slight asymmetries can be discerned in the latter, these asymmetries are considerably smaller than those observed in finite-volume predictions [18, 17]). The stagnation-point Stanton number in the MDG-ICE( $\mathcal{P}_5/\mathcal{P}_4$ ) solution is approximately 0.0077.

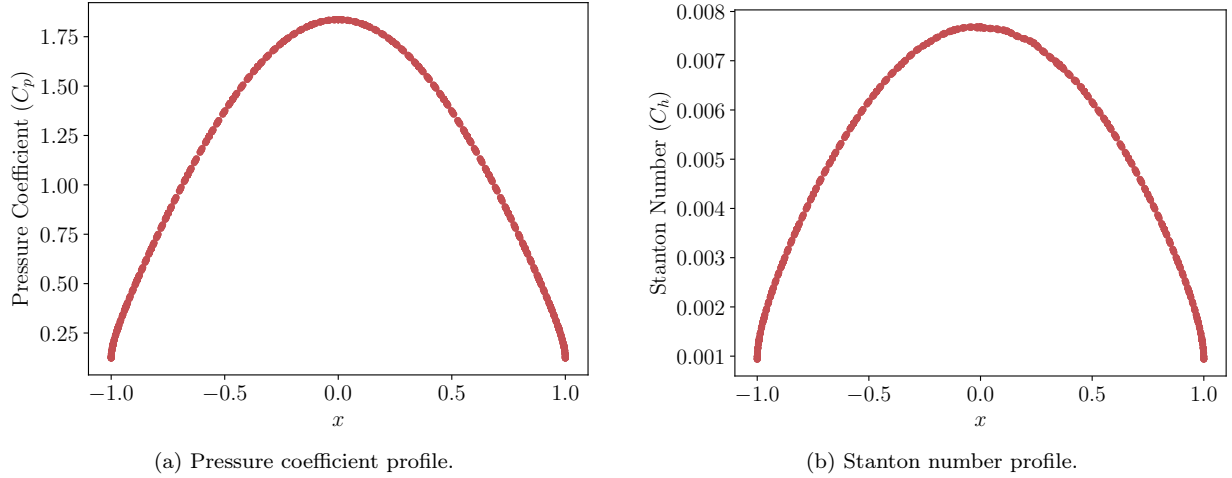


Figure 5.28: Surface profiles of pressure coefficient and Stanton number for the isoparametric MDG-ICE( $\mathcal{P}_4$ ) and subparametric MDG-ICE( $\mathcal{P}_5/\mathcal{P}_4$ ) solutions to three-dimensional Mach 17.6 flow over a cylinder at  $\text{Re} = 376,930$ . Pressure and heat-flux values at all auxiliary-variable degrees of freedom along the cylinder wall are shown. The initial grid has an irregular topology.

#### 5.4. Mach 5 flow over three-dimensional sphere

In our final test case, we compute steady Mach 5 laminar flow over a hemisphere in three spatial dimensions. Only one quarter of the hemisphere, which is of unit radius, is considered due to the memory footprint and computational cost of the linear solver. The Reynolds number (based on the sphere radius) is  $3.775 \times 10^6$ . The sphere boundary is an isothermal no-slip wall with temperature  $T_{\text{wall}} = 1.308T_{\infty}$ . These conditions are similar to those considered by Blottner [50], who employed an axisymmetric solver, and in the 2022 High-Fidelity CFD Workshop [51, 52], except the Reynolds number here is four times higher. At the freestream conditions by Blottner [50], large-scale asymmetries and mesh imprinting have been observed in three-dimensional finite volume and finite element solutions [52, 53, 54], even with structured hexahedral grids. Freestream conditions are imposed at the inflow boundary, defined as a quarter hemisphere with radius 2.3 times larger than that of the spherical body. Extrapolation is applied at the outflow boundary.

Continuation in Reynolds number is employed. Figure 5.29 presents the initial 7650-cell tetrahedral grid and an isoparametric DG( $\mathcal{P}_2$ ) solution at  $\text{Ma} = 5, \text{Re} = 100$ , which is used to initialize the MDG-ICE continuation with isoparametric  $\mathcal{P}_3$  elements. The sphere surface and the  $y = 0$  and  $z = 0$  planes are displayed. The freestream flow is in the  $-x$ -direction. Mesh imprinting along the sphere boundary and a highly diffused shock are observed in the DG solution. Given the cost of the LDLT linear solver, to maximize efficiency, the initial mesh is generated such that the azimuthal resolution is higher near the stagnation line than elsewhere. Furthermore, the wall-normal resolution is decreased near the inflow boundary. We also find that as the Reynolds number is increased, due to higher gradients at the shock than at the boundary layer, the solver tends to move cells from the near-wall region to the vicinity of the shock. To alleviate this loss of boundary-layer resolution, a very thin layer of cells is constructed adjacent to the wall. This issue can likely be resolved with localized artificial dissipation (to reduce gradients at the shock), a robust remeshing strategy, and/or local  $p$ -refinement, all of which will be pursued in the future. Nevertheless, we note that building an initial grid with additional resolution near the boundary surface is significantly simpler than constructing a grid with the required near-wall resolution while simultaneously aligning the grid interfaces with shocks, whose locations are generally unknown a priori. With our planned advancements to the MDG-ICE formulation (including a more efficient linear-solver strategy), we will consider the full hemispherical domain, as well as an initially irregular topology, in future work.

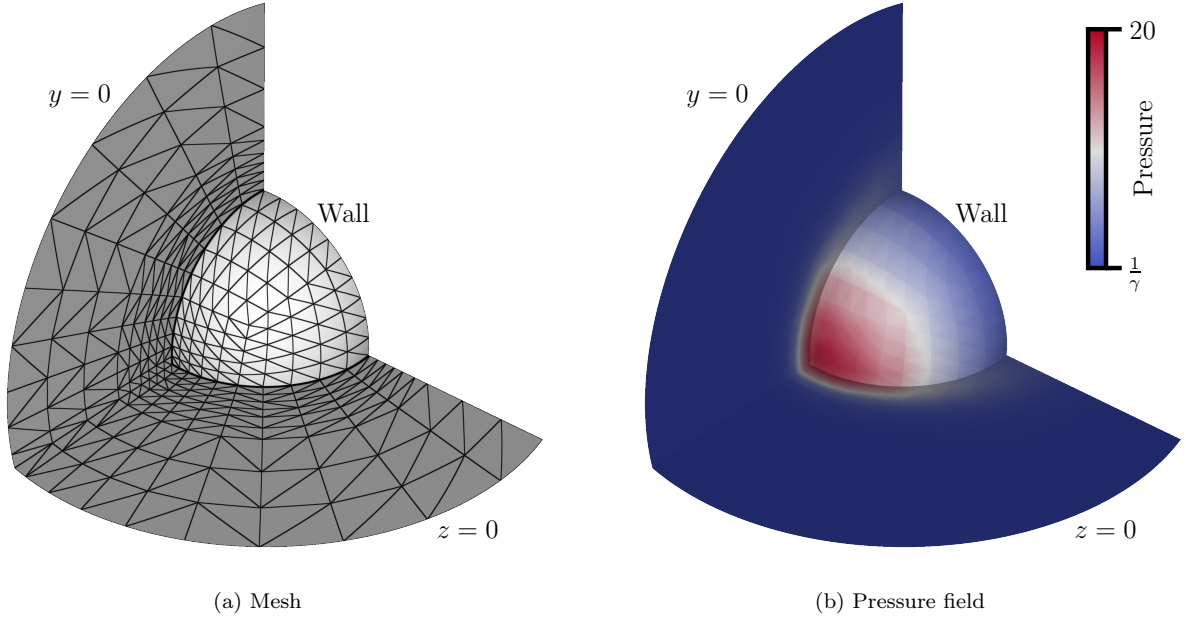


Figure 5.29: Isoparametric  $DG(\mathcal{P}_2)$  solution at  $Ma = 5, Re = 100$  on 7650 tetrahedral cells. This solution is used as the initial condition for the MDG-ICE continuation strategy. The sphere surface and the  $y = 0$  and  $z = 0$  planes are displayed. The freestream flow is in the  $-x$ -direction.

Successive increases in the Reynolds number leads to the appearance of temperature undershoots that are especially difficult to dampen in this problem in the absence of artificial dissipation. As in Section 5.3.2, to reduce these instabilities, we employ the alternative least-squares MDG-ICE formulation with optimal test functions [3]. After reaching the final Reynolds number, we perform two global  $p$ -refinements of the state and auxiliary-variable approximations while retaining the alternative least-squares MDG-ICE formulation. Figure 5.30 displays the final subparametric MDG-ICE( $\mathcal{P}_5/\mathcal{P}_3$ ) solution at  $Ma = 5, Re = 3.775 \times 10^6$ . To reduce the number of unnecessary elements in the freestream region, we project the inflow boundary to a quarter hemisphere of radius 2.15. Cell collapses [29] are then performed to remove invalid cells, resulting in 7161 elements. The final grid is shown in Figure 5.30a. The surface mesh is noticeably coarse. The pressure field and surface heat-flux profile, presented in Figures 5.30b and 5.30c, respectively, are free from mesh imprinting and spurious oscillations. Figure 5.30d provides a zoomed-in view of the temperature field along the  $z = 0$  plane. The temperature gradient in the boundary layer can be observed. The viscous shock resembles a true discontinuity, and the cells resolving the shock cannot be individually discerned. Nevertheless, grid validity is maintained. Note the closer proximity of the shock to the boundary layer than in the cylinder problem, despite a lower Mach number, which helps explain the aforementioned issue in which the solver moves grid points from the boundary layer to the shock.

The convergence history for the subparametric MDG-ICE( $\mathcal{P}_5/\mathcal{P}_3$ ) solution is presented in Figure 5.31. The initial residual is already low since we restart from a subparametric MDG-ICE( $\mathcal{P}_4/\mathcal{P}_3$ ) calculation. Figure 5.32 display profiles of temperature and pressure along the stagnation line. The stagnation point is located at  $x = -1$ . The stagnation-line quantities are plotted on a per-cell basis, such that only points within the same cell are connected. Again, it is very difficult to capture the interior of the extremely thin viscous shock using the employed line sampler, which explains why the shock is presented as a discontinuity. These results further exemplify the sharpness of the shock profile and the absence of spurious artifacts in the solution.

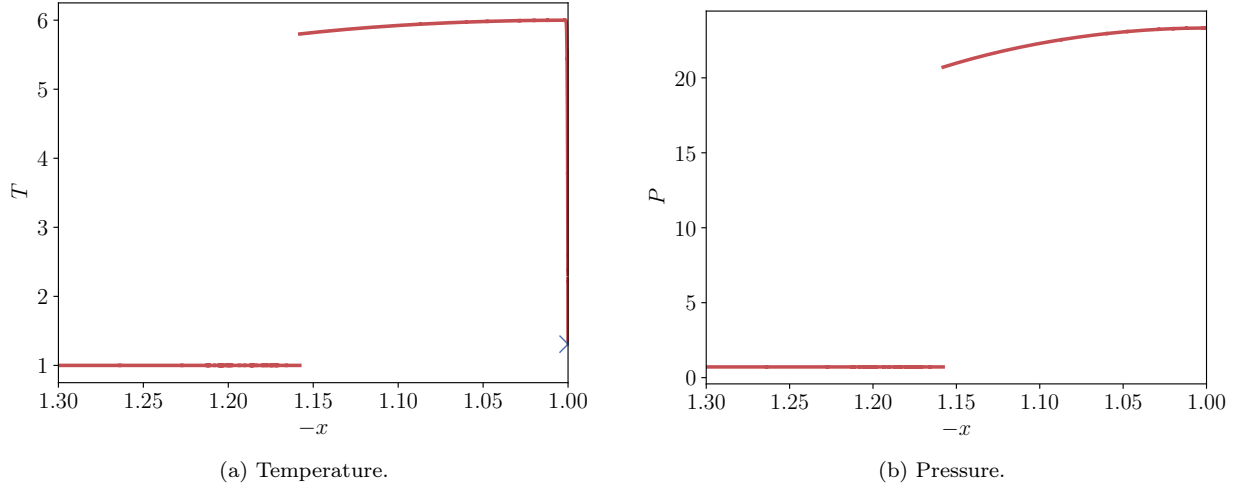


Figure 5.32: Stagnation-line profiles of temperature and pressure obtained with the MDG-ICE solution computed using 7161  $\mathcal{P}_5/\mathcal{P}_3$  subparametric triangle elements for three-dimensional Mach 5 flow over a sphere at  $\text{Re} = 3.775 \times 10^6$ . The stagnation point is located at  $x = -1$ . The stagnation-line quantities are plotted on a per-cell basis, such that only points within the same cell are connected. The exact stagnation-point temperature,  $T = 1.308$ , is marked with the symbol  $\times$ .

Figure 5.33 presents the streamwise variation of surface pressure and heat flux evaluated at all degrees of freedom corresponding to  $\Sigma_h$  for subparametric MDG-ICE( $\mathcal{P}_4/\mathcal{P}_3$ ) and MDG-ICE( $\mathcal{P}_5/\mathcal{P}_3$ ) solutions. The surface pressure is essentially perfectly symmetric. Noticeable asymmetries in the heat flux near the stagnation point for the MDG-ICE( $\mathcal{P}_4/\mathcal{P}_3$ ) solution are observed. These asymmetries are significantly reduced in the MDG-ICE( $\mathcal{P}_5/\mathcal{P}_3$ ) solution, resulting in a highly symmetric heat-flux profile. Note that interaction between the symmetry boundaries near the stagnation point may be a partial source of the small asymmetries. The stagnation-point Stanton number in the MDG-ICE( $\mathcal{P}_5/\mathcal{P}_3$ ) solution is approximately 0.00167, which agrees well with the value of 0.00159 obtained using the correlation by Fay and Riddell [55]. These results demonstrate the ability of MDG-ICE, combined with the enhanced optimization solver introduced in this work, to produce very accurate surface heating predictions even in the presence of considerable misalignment between the grid and the high-gradient features.

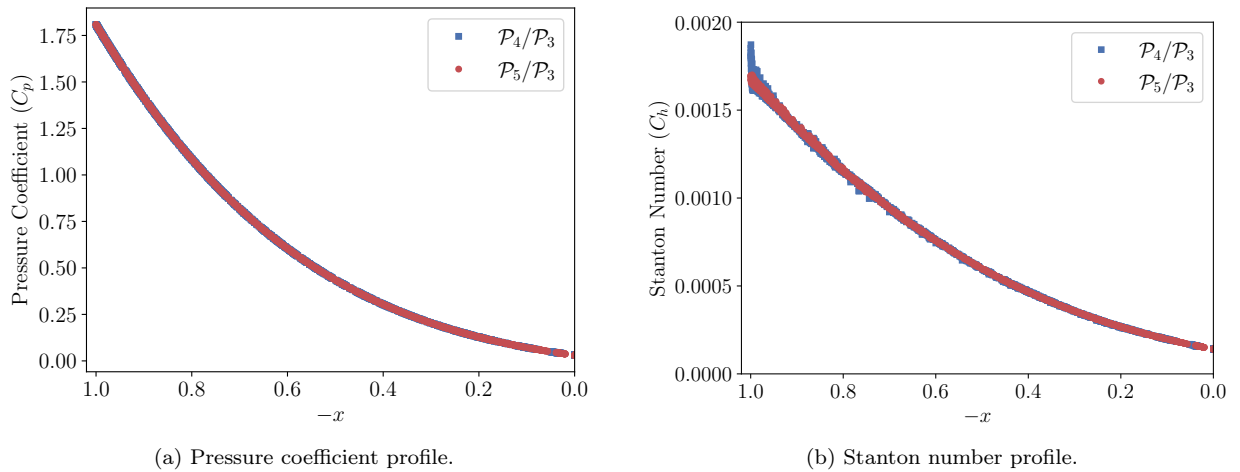


Figure 5.33: Streamwise variation of surface pressure and surface heat flux for the subparametric MDG-ICE( $\mathcal{P}_4/\mathcal{P}_3$ ) and MDG-ICE( $\mathcal{P}_5/\mathcal{P}_3$ ) solutions to three-dimensional Mach 5 flow over a sphere at  $\text{Re} = 3.775 \times 10^6$ . Pressure and heat-flux values at all auxiliary-variable degrees of freedom along the sphere wall are shown. The stagnation point is located at  $x = -1$ .

## 6. Conclusions and future work

We introduced an enhanced optimization solver for the moving discontinuous Galerkin method with interface condition enforcement (MDG-ICE), which automatically fits discontinuous and high-gradient features without a priori information via curvilinear  $r$ -adaptivity in both space and time. Specifically, to overcome the major bottleneck of frequent cell degeneration, we developed an anisotropic, locally adaptive penalty technique for the Levenberg-Marquardt method previously employed in [2]. The proposed MDG-ICE formulation, without any explicit stabilization mechanisms, was applied to three test cases involving sharp yet smooth gradients: Burgers viscous shock formation in space-time, Mach 17.6 viscous flow over a circular half-cylinder in two and three dimensions, and Mach 5 flow over a three-dimensional sphere. We used simplicial grids in order to evaluate the ability of the developed MDG-ICE formulation to obtain symmetric surface heat-flux profiles in the presence of strong misalignment between the grid and both the shock and boundary layer, which is considerably challenging for conventional numerical methods. Oscillation-free solutions and highly symmetric heating predictions were achieved.

Although the results presented in this work are very promising and demonstrate how MDG-ICE can significantly alleviate the burden of mesh generation on the user, additional advancements are needed in order to more fully realize its potential. Specifically, we plan to incorporate localized artificial dissipation (either only during intermediate iterations or in minimal amounts in the final solution), time marching via space-time MDG-ICE, local  $p$ -adaptivity, automatic selection and adjustment of regularization and other solver parameters [34, 12], and further improvements to the optimization solver that were originally proposed for the baseline Levenberg-Marquardt method [34]. In addition, we will integrate metric-based mesh regeneration/adaptation strategies into the solver, potentially utilizing the mesh-implied metric naturally produced by an MDG-ICE solution, which should already yield small element length scales at high-gradient features. These developments will likely accelerate convergence, circumvent the need for continuation in Mach number and Reynolds number, and allow for even coarser initial grids. We will also explore approximating strong viscous shocks as inviscid discontinuities as an intrinsic feature of the solver (i.e., without the use of ad hoc strategies); layers of high-aspect-ratio cells would then no longer be required since discontinuous shocks can simply be fit along grid interfaces, as in the inviscid setting [1]. Finally, the efficiency of solving the linear system will be improved.

## Acknowledgments

This work is sponsored by the Office of Naval Research through the Naval Research Laboratory 6.1 Computational Physics Task Area and by Dr. Eric Marineau of the Hypersonic Aerothermodynamics, High-Speed Propulsion and Materials Program of ONR Code 35.

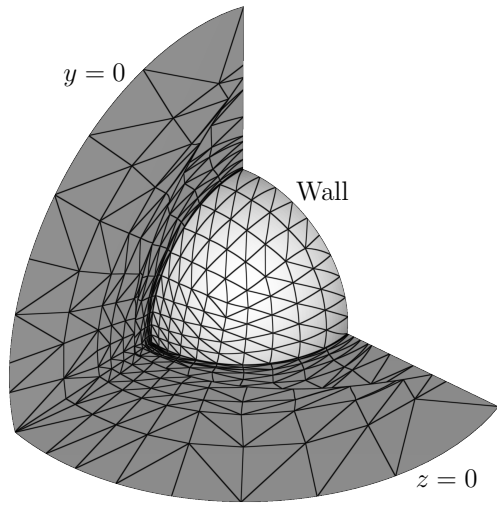
## References

- [1] A. Corrigan, A. Kercher, D. Kessler, A moving discontinuous Galerkin finite element method for flows with interfaces, *International Journal for Numerical Methods in Fluids* 89 (9) (2019) 362–406. doi:10.1002/fld.4697.
- [2] A. Kercher, A. Corrigan, D. Kessler, The moving discontinuous Galerkin finite element method with interface condition enforcement for compressible viscous flows, *International Journal for Numerical Methods in Fluids* 93 (5) (2021) 1490–1519. doi:10.1002/fld.4939.
- [3] A. Kercher, A. Corrigan, A least-squares formulation of the moving discontinuous Galerkin finite element method with interface condition enforcement, *Computers & Mathematics with Applications* 95 (2021) 143–171. doi:10.1016/j.camwa.2020.09.012.
- [4] W. H. Reed, T. Hill, *Triangular mesh methods for the neutron transport equation*, Tech. rep., Los Alamos Scientific Lab., N. Mex.(USA) (1973).
- [5] B. Cockburn, G. Karniadakis, C.-W. Shu, *The development of discontinuous Galerkin methods*, in: *Discontinuous Galerkin Methods*, Springer, 2000, pp. 3–50.
- [6] A. Majda, *Compressible fluid flow and systems of conservation laws in several space variables*, Springer Science & Business Media, 2012. doi:10.1007/978-1-4612-1116-7.
- [7] E. Ching, Y. Lv, P. Gnoffo, M. Barnhardt, M. Ihme, Shock capturing for discontinuous Galerkin methods with application to predicting heat transfer in hypersonic flows, *Journal of Computational Physics* 376 (2018) 54–75. doi:10.1016/j.jcp.2018.09.016.

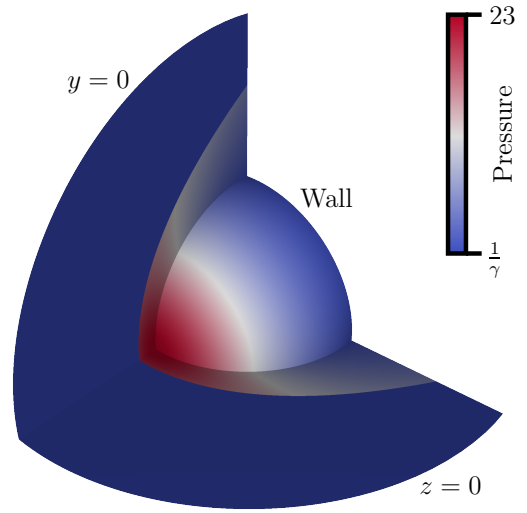
- [8] G. Moretti, Thirty-six years of shock fitting, *Computers & Fluids* 31 (4) (2002) 719–723. doi:10.1016/S0045-7930(01)00072-X.
- [9] M. Salas, *A shock-fitting primer*, CRC Press, 2009.
- [10] M. Salas, A brief history of shock-fitting, in: *Computational Fluid Dynamics 2010*, Springer, 2011, pp. 37–53.
- [11] M. Zahr, P.-O. Persson, An optimization-based approach for high-order accurate discretization of conservation laws with discontinuous solutions, *Journal of Computational Physics* 365 (2018) 105–134. doi:10.1016/j.jcp.2018.03.029.
- [12] M. Zahr, A. Shi, P.-O. Persson, Implicit shock tracking using an optimization-based high-order discontinuous Galerkin method, *Journal of Computational Physics* 410 (2020) 109385. doi:10.1016/j.jcp.2020.109385.
- [13] A. Shi, P.-O. Persson, M. J. Zahr, Implicit shock tracking for unsteady flows by the method of lines, *Journal of Computational Physics* 454 (2022) 110906.
- [14] T. Huang, M. Zahr, A robust, high-order implicit shock tracking method for simulation of complex, high-speed flows, *Journal of Computational Physics* 454 (2022) 110981.
- [15] T. Huang, C. J. Naudet, M. J. Zahr, High-order implicit shock tracking boundary conditions for flows with parametrized shocks, *Journal of Computational Physics* (2023) 112517.
- [16] H. Luo, G. Absillis, R. Nourgaliev, A moving discontinuous Galerkin finite element method with interface condition enforcement for compressible flows, *Journal of Computational Physics* 445 (2021) 110618.
- [17] I. Nompelis, T. Drayna, G. Candler, Development of a hybrid unstructured implicit solver for the simulation of reacting flows over complex geometries, in: *34th AIAA Fluid Dynamics Conference and Exhibit*, 2004, p. 2227, AIAA-2004-2227. doi:10.2514/6.2004-2227.
- [18] P. Gnoffo, J. White, Computational aerothermodynamic simulation issues on unstructured grids, in: *37th AIAA Thermophysics Conference*, 2004, p. 2371, AIAA-2004-2371. doi:10.2514/6.2004-2371.
- [19] G. Candler, D. Mavriplis, L. Trevino, Current status and future prospects for the numerical simulation of hypersonic flows, in: *AIAA (Ed.), 47th AIAA Aerospace Sciences Meeting including The New Horizons Forum and Aerospace Exposition*, 2009, AIAA-2009-0153. doi:10.2514/6.2009-0153.
- [20] K. J. Fidkowski, A simplex cut-cell adaptive method for high-order discretizations of the compressible Navier-Stokes equations, Ph.D. thesis, Massachusetts Institute of Technology (2007).
- [21] T. A. Oliver, A high-order, adaptive, discontinuous Galerkin finite element method for the Reynolds-Averaged Navier-Stokes equations, Ph.D. thesis, Massachusetts Institute of Technology (2008).
- [22] M. Ceze, K. J. Fidkowski, Constrained pseudo-transient continuation, *International Journal for Numerical Methods in Engineering* 102 (11) (2015) 1683–1703.
- [23] P. A. Gnoffo, Planetary-entry gas dynamics, *Annual Review of Fluid Mechanics* 31 (1) (1999) 459–494.
- [24] K. Levenberg, A method for the solution of certain non-linear problems in least squares, *Quarterly of applied mathematics* 2 (2) (1944) 164–168. doi:10.1090/qam/10666.
- [25] D. Marquardt, An algorithm for least-squares estimation of nonlinear parameters, *Journal of the society for Industrial and Applied Mathematics* 11 (2) (1963) 431–441. doi:10.1137/0111030.
- [26] E. Ching, M. Ihme, Efficient projection kernels for discontinuous Galerkin simulations of disperse multiphase flows on arbitrary curved elements, *Journal of Computational Physics* 435 (2021) 110266. doi:10.1016/j.jcp.2021.110266.
- [27] T. Toulorge, C. Geuzaine, J. Remacle, J. Lambrechts, Robust untangling of curvilinear meshes, *Journal of Computational Physics* 254 (2013) 8–26.
- [28] F. Alauzet, A changing-topology moving mesh technique for large displacements, *Engineering with Computers* 30 (2) (2014) 175–200.
- [29] R. Löhner, *Applied CFD Techniques*, J. Wiley & Sons, 2008.
- [30] Z. Xie, R. Sevilla, O. Hassan, K. Morgan, The generation of arbitrary order curved meshes for 3D finite element analysis, *Computational Mechanics* 51 (2013) 361–374.
- [31] D. Moxey, D. Ekelschot, Ü. Keskin, S. Sherwin, J. Peiró, High-order curvilinear meshing using a thermo-elastic analogy, *Computer-Aided Design* 72 (2016) 130–139.
- [32] J. Marcon, A. Garai, M. Denison, S. Murman, An adjoint elasticity solver for high-order mesh deformation, in: *AIAA Scitech 2021 Forum*, 2021, p. 1238.
- [33] A. Gargallo-Peiró, X. Roca, J. Peraire, J. Sarrate, Distortion and quality measures for validating and generating high-order tetrahedral meshes, *Engineering with Computers* 31 (3) (2015) 423–437.
- [34] M. K. Transtrum, J. P. Sethna, Improvements to the Levenberg-Marquardt algorithm for nonlinear least-squares minimization, arXiv preprint arXiv:1201.5885 (2012).
- [35] C. Geuzaine, J.-F. Remacle, Gmsh: A three-dimensional finite element mesh generator with built-in pre- and post-processing facilities, *International Journal for Numerical Methods in Engineering* (79(11)) (2009) 1310–1331.
- [36] P. Amestoy, I. S. Duff, J. Koster, J.-Y. L'Excellent, A fully asynchronous multifrontal solver using distributed dynamic scheduling, *SIAM Journal on Matrix Analysis and Applications* 23 (1) (2001) 15–41.
- [37] P. Amestoy, A. Buttari, J.-Y. L'Excellent, T. Mary, Performance and scalability of the block low-rank multifrontal factorization on multicore architectures, *ACM Transactions on Mathematical Software* 45 (2019) 2:1–2:26.
- [38] S. Balay, W. D. Gropp, L. C. McInnes, B. F. Smith, Efficient management of parallelism in object oriented numerical software libraries, in: E. Arge, A. M. Bruaset, H. P. Langtangen (Eds.), *Modern Software Tools in Scientific Computing*, Birkhäuser Press, 1997, pp. 163–202.
- [39] S. Balay, S. Abhyankar, M. F. Adams, S. Benson, J. Brown, P. Brune, K. Buschelman, E. Constantinescu, L. Dalcin, A. Dener, V. Eijkhout, J. Faibussowitsch, W. D. Gropp, V. Hapla, T. Isaac, P. Jolivet, D. Karpeev, D. Kaushik, M. G. Knepley, F. Kong, S. Kruger, D. A. May, L. C. McInnes, R. T. Mills, L. Mitchell, T. Munson, J. E. Roman, K. Rupp, P. Sanan, J. Sarich, B. F. Smith, S. Zampini, H. Zhang, H. Zhang, J. Zhang, *PETSc/TAO users manual*, Tech. Rep.



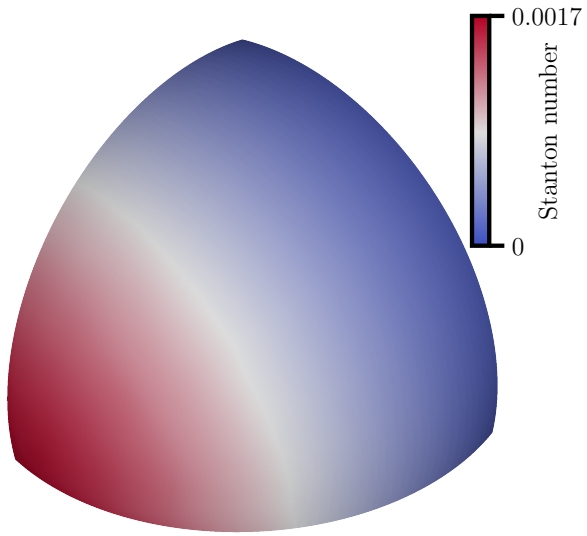
- ANL-21/39 - Revision 3.20, Argonne National Laboratory (2023). doi:10.2172/1968587.
- [40] G. Barter, D. Darmofal, Shock capturing with PDE-based artificial viscosity for DGFEM: Part I. formulation, *Journal of Computational Physics* 229 (5) (2010) 1810–1827. doi:10.1016/j.jcp.2009.11.010.
  - [41] R. F. Johnson, A. D. Kercher, A conservative discontinuous Galerkin discretization for the chemically reacting Navier-Stokes equations, *Journal of Computational Physics* 423 (2020) 109826. doi:10.1016/j.jcp.2020.109826.
  - [42] E. Ching, A. Kercher, A. Corrigan, Anisotropic mesh modifications for the moving discontinuous Galerkin method with interface condition enforcement for robust simulations of high-speed viscous flows, in: *Eleventh International Conference on Computational Fluid Dynamics (ICCFD11)*, Maui, Hawaii, 2022, ICCFD11-0305.
  - [43] K. Kitamura, E. Shima, Towards shock-stable and accurate hypersonic heating computations: A new pressure flux for AUSM-family schemes, *Journal of Computational Physics* 245 (2013) 62–83.
  - [44] Y. Lv, M. Ihme, Entropy-bounded discontinuous Galerkin scheme for Euler equations, *Journal of Computational Physics* 295 (2015) 715–739.
  - [45] Y. Jiang, H. Liu, Invariant-region-preserving DG methods for multi-dimensional hyperbolic conservation law systems, with an application to compressible Euler equations, *Journal of Computational Physics* 373 (2018) 385–409.
  - [46] E. Ching, R. Johnson, A. Kercher, Positivity-preserving and entropy-bounded discontinuous Galerkin method for the chemically reacting, compressible Euler equations. Part I: The one-dimensional case, *arXiv preprint arXiv:2211.16254* <https://arxiv.org/abs/2211.16254> (2022).
  - [47] L. Demkowicz, J. Gopalakrishnan, A class of discontinuous Petrov–Galerkin methods. Part I: The transport equation, *Computer Methods in Applied Mechanics and Engineering* 199 (23–24) (2010) 1558–1572. doi:10.1016/j.cma.2010.01.003.
  - [48] L. Demkowicz, J. Gopalakrishnan, A class of discontinuous Petrov–Galerkin methods. II. Optimal test functions, *Numerical Methods for Partial Differential Equations* 27 (1) (2011) 70–105. doi:10.1002/num.20640.
  - [49] L. Demkowicz, J. Gopalakrishnan, Discontinuous Petrov-Galerkin (DPG) method, Tech. Rep. 15-20, ICES, retrieved from <https://www.oden.utexas.edu/media/reports/2015/1520.pdf> (October 2015).
  - [50] F. Blottner, Accurate Navier-Stokes results for the hypersonic flow over a spherical nosetip, *Journal of spacecraft and Rockets* 27 (2) (1990) 113–122. doi:10.2514/3.26115.
  - [51] T. Fisher, High fidelity CFD workshop 2021: High speed steady advanced case: Blottner sphere, NASA Langley Research Center Turbulence Modeling Resource [https://turbmodels.larc.nasa.gov/highfidelitycfid\\_{\\_}workshop2022.html](https://turbmodels.larc.nasa.gov/highfidelitycfid_{_}workshop2022.html) (2021).
  - [52] A. Murphy, R. Agarwal, Computational analysis of laminar steady hypersonic flow past Blottner sphere using ANSYS Fluent, in: *AIAA AVIATION 2023 Forum*, 2023, AIAA-2023-3847.
  - [53] B. Kirk, S. Bova, R. Bond, The influence of stabilization parameters in the SUPG finite element method for hypersonic flows, in: *48th AIAA Aerospace Sciences Meeting Including the New Horizons Forum and Aerospace Exposition*, 2010, AIAA-2010-1183.
  - [54] B. L. S. Couchman, Comparison of heat flux predictions over the Blottner cylinder and sphere., Tech. rep., Sandia National Lab. (SNL-NM), Albuquerque, NM (United States) (2018).
  - [55] J. Fay, F. Riddell, Theory of stagnation point heat transfer in dissociated air, *Journal of the Aerospace Sciences* 25 (2) (1958) 73–85.



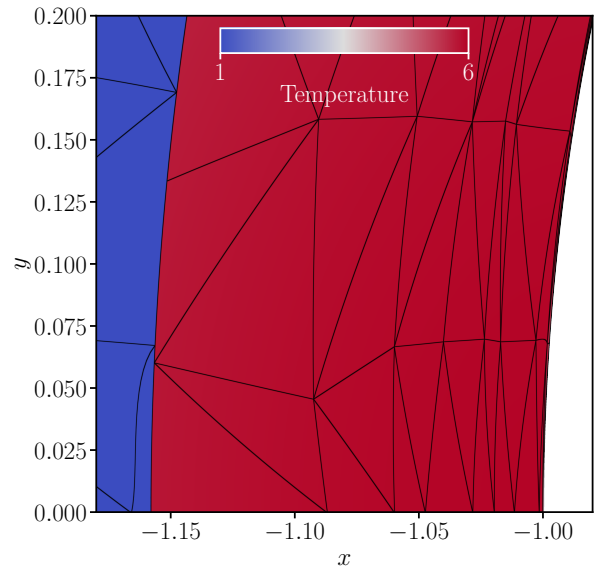
(a) Mesh.



(b) Pressure field.



(c) Surface heat flux.



(d) Zoomed-in view of temperature profile along  $z = 0$  plane.

Figure 5.30: Final grid and pressure field for the subparametric MDG-ICE( $\mathcal{P}_5/\mathcal{P}_3$ ) solution to hypersonic flow over a sphere at  $\text{Ma} = 5$ ,  $\text{Re} = 3.775 \times 10^6$ . In Figures 5.30a and 5.30b, the  $y = 0$  and  $z = 0$  planes and the sphere wall are displayed. The freestream flow is in the  $-x$ -direction.

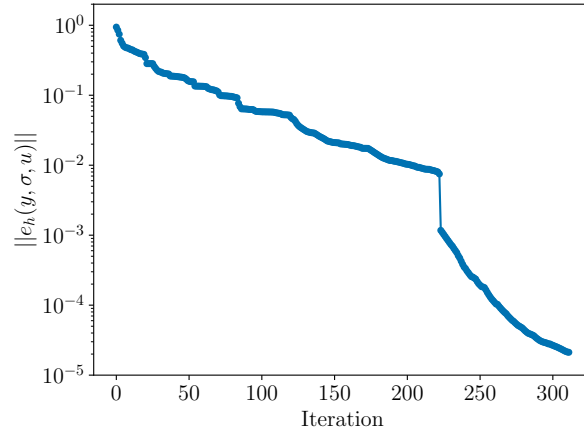


Figure 5.31: Nonlinear convergence history for the subparametric MDG-ICE( $\mathcal{P}_5/\mathcal{P}_3$ ) solution to Mach 5 flow over a sphere.